A tactile discrimination task to study neuronal dynamics in freely-moving mice

Filippo Heimburg*[,1], Nadin Mari Saluti*[,1], Josephine Timm*[,1,2], Avi Adlakha [3], Maria Helena Bortolozzo-Gleich[1], Jesús Martín-Cortecero[1], Melina Castelanelli[1], Matthias Klumpp[1], Lee Embray[1], Martin Both[1], Thomas Kuner[3] and Alexander Groh[1]

*first authors

[1] Institute for Physiology and Pathophysiology, Heidelberg University, 69120, Germany

[2] Current address: Institute for Experimental Epileptology and Cognition Research, University of Bonn, 53105, Germany

[3] Institute for Anatomy and Cell Biology, Heidelberg University, 69120, Germany

groh@uni-heidelberg.de (AG)

Abstract

Sensory discrimination tasks are valuable tools to study neuronal mechanisms of perception and learning. Most discrimination tasks for electrophysiological and imaging studies in rodents require the animals to be head-fixed. However, implementing neurophysiological recordings into more ethologically realistic settings with unrestrained animals has been challenging. Here, we introduce a whisker-dependent discrimination task for freely moving mice, integrating electrophysiology and calcium imaging with cellular resolution. In this go/no-go paradigm, male mice learned to discriminate aperture widths within days while foraging on a linear platform. The setup's versatility enables exploration into diverse behavioral aspects, including tactile discrimination thresholds, valence-dependent behavior, and cognitive flexibility following repeated task rule reversals. Rule learning was highly stereotypical, fast and reproducible across individual mice. Electrophysiological recordings revealed distributed tactile processing across the thalamocortical system, with subsets of units encoding both movement- and stimulus-related features. Sensory encoding was strongly modulated by behavioral state, with neurons tuned to locomotion, whisking, whisker angle and phase, head angle, and spatial position. By enabling simultaneous extracellular recordings and calcium imaging within the same freely moving paradigm, this approach allows for precise synchronization of neural activity with multiple behavioral readouts. This paradigm provides a versatile tool to elucidate neural mechanisms of cognition and sensory processing in naturalistic conditions.

Introduction

The rodent whisker system serves as a prevalent model for studying somatosensation in the mammalian brain, providing fundamental insights into the mechanisms of sensory perception, learning, and neuronal coding at the single neuron and synaptic levels [1–12]. Since the discovery of the whisker-to-cortex system [13], increasingly advanced experimental approaches have been devised to elucidate the biology and behavioral function of whiskers, while remaining compatible with high-resolution neurophysiological recordings. The most advanced current state-of-the-art approaches employ recordings in head-fixed mice or rats, while they learn to

report or discriminate sensory stimuli [6,14–19]. However, while the head-fixed approach presents the best current compromise between experimental control and biological relevance, head-fixed paradigms impose a limitation in accounting for a core ethological function of the whiskers: navigating mazes to search for food, which requires free head movements.

To overcome this limitation, we developed a go/no-go aperture discrimination task for mice inspired by earlier studies on rats [20,21], and combined the task with state-of-the-art single-unit electrophysiological recordings and miniscope imaging. We made modifications to the original design to accommodate rapid learning of multiple rules within an experimentally accessible timeframe in mice. The paradigm enables behavior that more closely resembles natural conditions (foraging in a freely moving apparatus) while allowing monitoring of decision-making processes, including licking, head movements, and whisker behavior. We show that neuronal activity can be monitored over the course of several learning stages in multiple regions of the whisker system using multi-site tetrode recordings and miniscope imaging in the same behavioral paradigm. We demonstrate that this paradigm can be used to study learning mechanisms on the behavioral and neuronal level, including insight-like learning, rule reversal and extinction as well as neural encoding of diverse internal and external world parameters.

Results

Tactile discrimination setup and learning paradigm

We developed an ethological paradigm in which freely moving mice learn to discriminate different aperture widths with their whiskers in order to collect food rewards. The behavioral apparatus included a linear track equipped with lick ports (LP) for reward delivery (condensed milk) and loudspeakers for punishment (white noise, 120 dB, random duration between 1 to 3 seconds), both situated at opposite ends of the track. To access the LPs, mice had to navigate through motorized apertures of varying widths (Fig. 1a). To ensure adult mice interacted with the aperture using their whiskers during the passage, we estimated the relevant range of aperture widths to be between 45 and 25 mm. Training sessions were done with ambient lights turned off and LEDs (overhead LEDs, backlights, beam brakes) operating in the infrared (IR) spectrum (850 nm), ensuring that mice did not use visual cues to discriminate apertures.

The session started when the mouse crossed the middle IR beam for the first time (Fig. 1a) during the approach to either of the two apertures. A trial started when one of the outer IR beams was crossed (Fig. 1a). Upon palpating the aperture with their whiskers, mice indicated their choice by either licking or not licking at the LP (Suppl. Video 1-3). The general rule logic for scoring the choices and triggering the outcomes was as follows (Fig. 1b, Table 2): licking in response to the go aperture was considered a “hit” and resulted in reward delivery, while not licking was considered a “miss” and resulted in no outcome. Licking in response to the no-go aperture was considered a “false alarm (FA)” and resulted in punishment, while not licking was considered a “correct rejection (CR)” with no outcome. In a later training stage, we introduced a “neutral” aperture which was equidistant to the go and no-go aperture (i.e., 35 mm) and which resulted in no outcome and no scoring.

Prior to training, mice underwent controlled food intake for two days with a target body weight of 85–90 % of the initial body weight, which was maintained throughout the later training stages

to increase motivation. During this period, mice underwent handling and LP training in their home cage. LP training was conducted with a dummy LP connected to a syringe via a flexible tube, and condensed milk was dispensed manually upon licking. The training consisted of multiple training stages with stage-specific criteria required to progress to the next stage (Fig. 1c, Table 2). During the habituation stage, in which the apertures remained in the go-state, mice learned to alternate between the two LPs and collect rewards. Habituation was completed after four sessions and at least fifty lick trials, after which mice progressed to learn the initial rule, wherein one aperture was linked to reward and a second aperture was linked to punishment. After mice learned the initial rule, they were trained for eight more sessions with the additional neutral aperture. The neutral stage was followed by the reversed rule stage, with reward and punishment contingencies reversed and the neutral aperture removed. In the final stage, the learned behavior was extinguished by randomizing both the apertures and the outcome. The mice's ability to differentiate between aperture widths was assessed using the discriminability index d-prime (d') (Fig. 1d, first column).

Operation of the setup and data acquisition was controlled by Syntalos [22]. Behavioral data was written into an event list which contained the aperture state and data from the three IR beams and the two LPs (Fig. 1a). Data from the event list was used to calculate the performance (Fig. 1d, first column). Recordings from the two high-speed cameras above each LP were triggered when the mouse crossed the outer beam sensors and ended upon the mouse licking or crossing the center IR beam (Suppl. Video 1, 2). These videos were used to extract whisker-aperture contact times and whisker angles using DeepLabCut [23] (Fig. 1d, second column). An overview camera continuously recorded the entire track (Fig. 1a, Suppl. Video 3) and was used for tracking head-movements as well as mouse location and speed. Syntalos additionally operated and archived the multi-channel electrode recordings and miniscope calcium imaging data (Fig. 1d, last two columns).

111

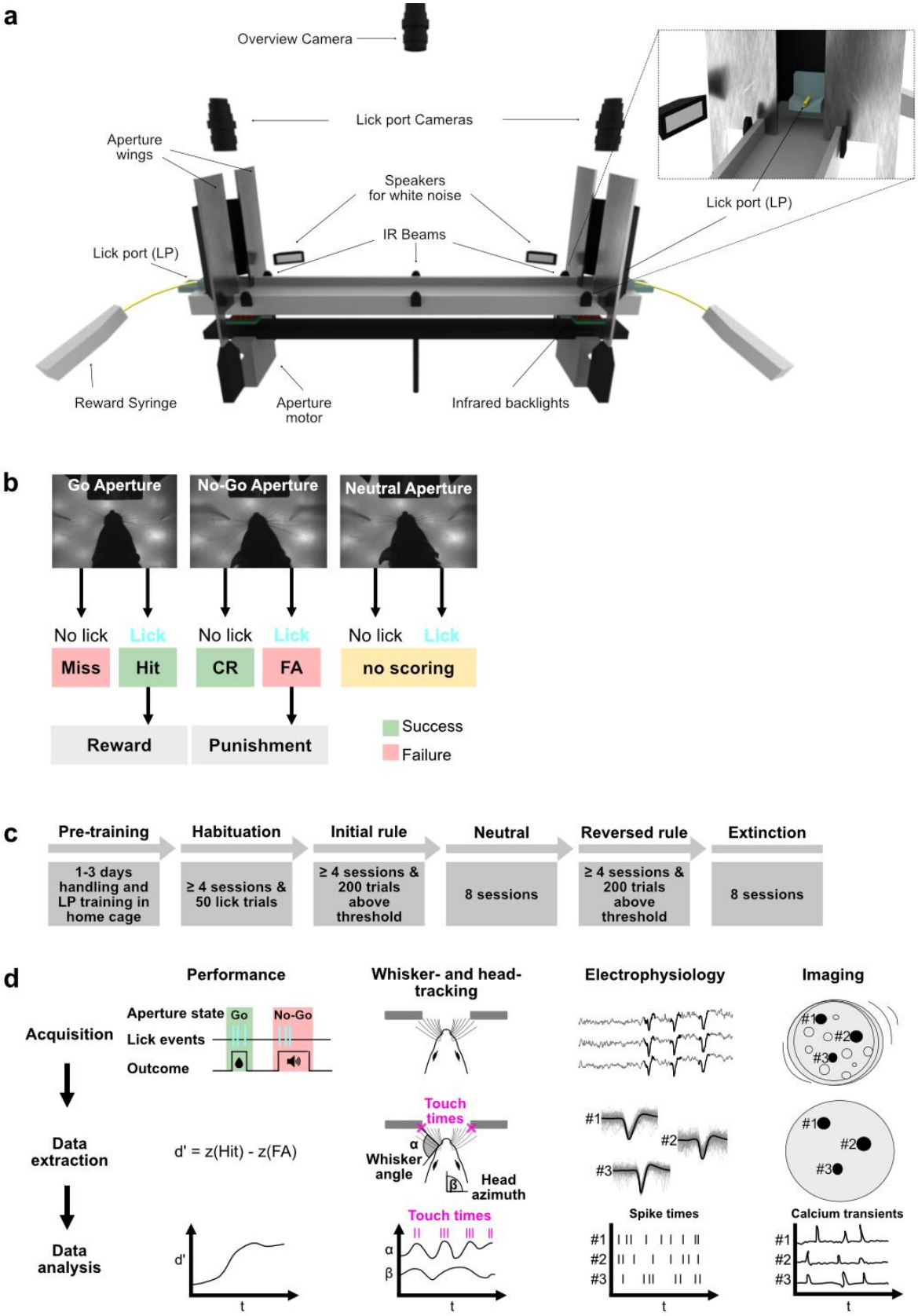
a
Overview Camera
Lick port Cameras
Aperture wings
Speakers for white noise
IR Beams
Lick port (LP)
Lick port (LP)
Reward Syringe
Aperture motor
Infrared backlights
b
Go Aperture
No-Go Aperture
Neutral Aperture
No lick
Lick
Miss
Hit
CR
FA
no scoring
Reward
Punishment
Success
Failure
c
Pre-training
1-3 days handling and LP training in home cage
Habituation
≥ 4 sessions & 50 lick trials
Initial rule
≥ 4 sessions & 200 trials above threshold
Neutral
8 sessions
Reversed rule
≥ 4 sessions & 200 trials above threshold
Extinction
8 sessions
d
Performance
Whisker- and head-tracking
Electrophysiology
Imaging
Acquisition
Aperture state
Go
No-Go
Lick events
Outcome
Data extraction
d' = z(Hit) - z(FA)
Data analysis
d'
t
Touch times
α
Whisker angle
β
Head azimuth
Touch times
Spike times
Calcium transients
#1
#2
#3

112

Fig. 1: Tactile discrimination setup and learning paradigm. **a:** Display of the whisker-discrimination setup, created with Blender v2.9 (files can be found here: https://github.com/GrohLab/A-tactile-discrimination-task-to-study-neuronal-dynamics-in-freely-moving-mice [24]). **b:** Rule logic for scoring the choices and triggering the outcomes. **c:** Training scheme with different learning stages and criteria to move to the next stage. **d:** Overview of data acquisition and analysis pipeline for the analysis of task performance, whisker-aperture touch times, head-tracking, single-unit spike times and calcium transients.

Mice learn to discriminate apertures with their whiskers and learn different task rules

We trained a cohort of 12 mice on the basic training scheme as illustrated in Fig. 1c. First we examined lick rates for the different apertures across all subjects over the course of learning. The analysis demonstrated a gradual increase in lick rates for the rewarded aperture and a steep decrease in lick rates for the punished aperture (Fig. 2a). This divergence in lick rates during the initial learning stage indicates the onset of the learning process, which is also reflected in the population success rate (Fig. 2b). Individual analysis revealed that 5 of the 12 animals increased their success rates in no-go trials by a factor of five at around 60 % of the stage progression, suggesting a moment of insight previously described by Rosenberg et al., 2021 [25]. On average, mice needed 471 trials (± 128) to surpass the expert-level performance threshold (d' = 1.65) (Fig. 2c). For extended analyses of d' and success rates over sessions see Fig. S1a, b. Throughout the learning process, mice more than tripled their activity rate from approximately 20 trials per session in the first four sessions to 60 trials per session in the last four sessions (Fig. S1c).

After reaching the expert-level criterion (4 sessions and 200 trials above expert threshold), mice were trained in the neutral stage, where the lick rates in response to neutral aperture trials were intermediate between the go and no-go lick rates (Fig. 2a, middle), suggesting that the mice can differentiate between more than two stimuli.

In the reversal stage, licking at the wide aperture resulted in punishment and licking at the narrow aperture resulted in reward. During the reversed rule stage, mice initially exhibited inverted lick rates, reflecting their adherence to the previously learned rule. Over time, they gradually adapted to the reversed rule, resulting in a shift toward the correct behavioral response. Notably, in both the initial- and the reversed rule stage, lick rates for the punished aperture dropped after approximately 60-70% of the learning progression (Fig. 2a), consistent with insight-like learning in the reversed stage (Fig. S1d). Notably, mice required more than twice the number of trials to learn the reversed rule in comparison to the initial rule (471 trials ± 127 vs. 1103 ± 256 trials, Fig. 2d). In agreement with slower reversal learning, the learning speed, estimated from the slope of a logistic fit of the d' progression, was more than two times slower compared to the initial learning (Fig. S1e).

We then investigated whether mice (n = 6) demonstrate faster relearning of previously learned rules. Indeed, during repeated rule reversals, mice relearned the rules within fewer trials compared to the first reversal (mean ± standard deviation, 1st reversal: 1078 ± 330 trials, 2nd reversal: 728 ± 144 trials, 3rd reversal: 701 ± 146 trials, Fig. 2d, S1f), indicating increased efficiency in relearning repeated rule reversals.

After reaching expert criterion in the reversed rule stage, mice underwent an extinction stage in order to extinguish the previously learned stimulus-outcome associations by randomizing both aperture states and outcomes in each trial (50% chance for “wide”, “narrow”, “reward” and “punishment”). During the extinction stage, mice changed their behavior within the first session, such that they always licked, regardless of the aperture state and outcome, resulting in a drop in the discrimination performance to chance level (Fig. 2e, S1g).

Further, we investigated the minimal aperture contrast that mice can robustly discriminate. We trained a cohort of eight animals on the previous stimulus set which has a contrast of 20 mm (wide = 45 mm; narrow = 25 mm). Subsequently, the contrast was reduced by steps of 4 mm and then by 2 mm. Animals were required to reach the expert-level criterion at each contrast before progressing to the next smaller contrast. We determined the smallest discriminable contrast at 6 mm, below which performance dropped below the expert-level performance threshold. At a contrast of 2 mm, performance dropped to chance level (Fig. 2f). Next, we trained three additional naive cohorts, each on a different contrast (12, 14, 16 mm), in order to determine the learning times for different contrasts. We found that animals trained on a larger contrast needed fewer trials to learn the rules compared to animals trained on a smaller contrast (Fig. 2g, S2). For the 16 mm contrast, mice required an average of 701 ± 110 trials (Fig. S2a, blue line) to reach expert-level performance, whereas those trained on 14 mm and 12 mm contrast required 1180 ± 215 trials (Fig. S2b, blue line) and 1356 ± 142 trials (Fig. S2c, blue line), respectively.

We next tested reversal learning for different contrasts. Again, compared to the initial rule stage, animals required more than twice as many trials to relearn the rule during the reversal stage (factor = 2.22, taking all contrasts into account). The factor between contrasts was not statistically different, suggesting that mice require about twice as many trials for reversal learning independently of the contrast. Specifically, during the reversal stage, mice required 1633 ± 356 trials to relearn the task with a 16 mm contrast (Fig. S2a, orange line) and 2260 ± 255 trials with a 14 mm contrast (Fig. S2b, orange line).

In summary, this paradigm can be used to train mice to discriminate apertures and to learn different task rules. Mice demonstrated the capacity to update their behavior to new reward-punishment contingencies during multiple reversal stages.

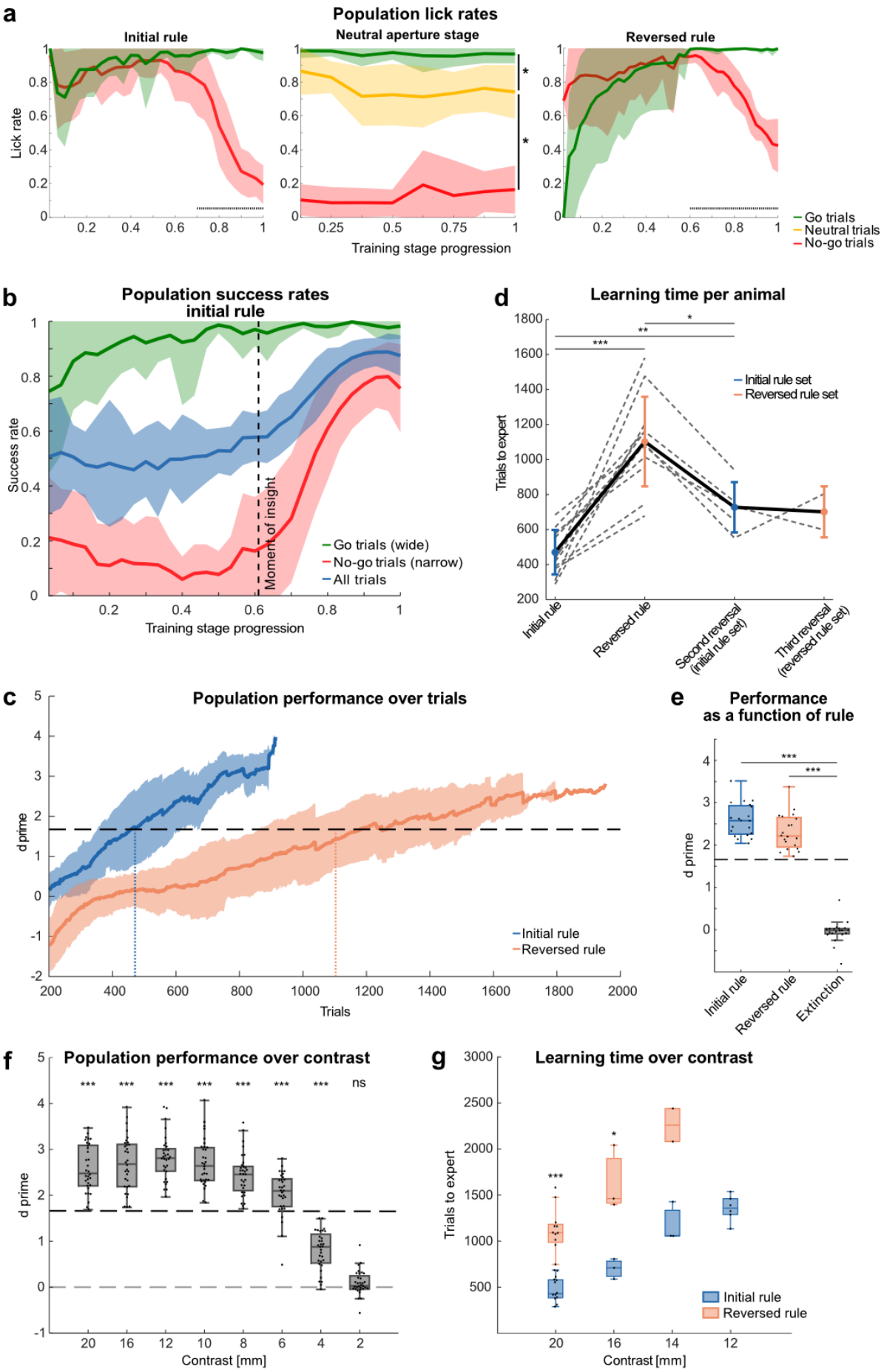
a
Population lick rates
Initial rule
Neutral aperture stage
Reversed rule
Lick rate
Training stage progression
Go trials
Neutral trials
No-go trials
b
Population success rates
initial rule
Success rate
Moment of insight
Go trials (wide)
No-go trials (narrow)
All trials
Training stage progression
d
Learning time per animal
Trials to expert
Initial rule set
Reversed rule set
Initial rule
Reversed rule
Second reversal (initial rule set)
Third reversal (reversed rule set)
c
Population performance over trials
d prime
Initial rule
Reversed rule
Trials
e
Performance as a function of rule
d prime
Initial rule
Reversed rule
Extinction
f
Population performance over contrast
d prime
Contrast [mm]
g
Learning time over contrast
Trials to expert
Initial rule
Reversed rule
Contrast [mm]

Fig. 2: Mice learn to discriminate apertures with their whiskers and learn different task rules. **a:** Mean lick rates from n = 12 mice across three different rule stages. Horizontal dashed lines indicate significant differences. **b:** Success rates over stage progression for Go- (Hit/(Hit+Miss)), No-go (CR/(CR+FA)) and all trials ((Hit+CR)/(Hit+Miss+CR+FA)) (n = 12 mice). Dashed line indicates "moment of insight", defined by a jump in success rate in no-go trials by a factor of five from one session to the next (n = 5 mice). **c:** Performance over trials for 20 mm contrast. Solid lines show mean d', calculated with a running window of the preceding 200 trials; shaded areas show standard deviation, horizontal dashed line indicates expert-level performance threshold (d' = 1.65); n = 12 mice). Animals reached expert-level performance after 471 trials in the initial rule stage and after 1103 trials in the reversed rule stage (dotted vertical lines). **d:** Learning times for initial-, 1st-, 2nd- and 3rd- rule reversal (dotted lines: individual animals; solid lines: means and standard deviation; n = 12 mice). **e:** Performance for initial rule, reversed rule and extinction. Horizontal dashed line indicates expert-level performance threshold (d' = 1.65). Performance was calculated from the last four sessions in the initial rule and reversed rule stage and the first four sessions in the extinction stage, each dot represents one session, n = 5 mice. **f:** Population performance for mice trained on a gradually decreasing contrast. Horizontal dashed lines indicate chance-level and expert-level performance thresholds (d' = 0 vs 1.65, respectively). Performance was calculated from the last four sessions in each contrast condition, each dot represents one session, n = 8 mice. **g:** Number of trials required to reach expert-levels for animals trained on different contrasts in the initial and reversed rule.

ns: $p > 0.05$, *: $p \leq 0.05$, **: $p \leq 0.01$ and ***: $p \leq 0.001$; **a:** Welch's t-test, **d, g:** paired t-test, **e:** repeated measures anova, **f:** one-sample t-test. For exact statistics see Supplementary Table 1.

Electrophysiological and optical recordings in freely moving mice during tactile discrimination

We explored the versatility of the setup to employ electrophysiological and imaging approaches in the same behavioral paradigm. Therefore, we first implanted tetrode arrays to record simultaneous unit-spiking activity from multiple areas of the somatosensory system in a cohort of 6 mice (Fig. 3a). Tetrode arrays were targeted to the barrel cortex (BC), ventral posteromedial nucleus (VPM), posterior medial complex (POm), and ventral zona incerta (ZIv) (Table 4). Analysis of the electrophysiological data in expert mice (d' ≥ 1.65), revealed significant modulation of neuronal firing rates following whisker-aperture contacts in all four brain regions (Fig. 3b). The onset latencies of these responses, measured as the time to the first significant deviation from baseline (see Methods for details), exhibited rapid recruitment of the recorded brain areas (Fig. 3c), supportive of correct targeting of the somatosensory pathway.

In addition to electrophysiology, we employed deep-brain calcium imaging (Fig. 3d). We chose the POm as the region of interest because of the recent attention on POm as a thalamic hub for higher cognitive functions [26–30]. To record in vivo calcium signals we expressed GCaMP6f in POm (Fig. S3). Mice were then trained to reach expert-level performance and somatic calcium signals were imaged with miniscopes attached to an implanted GRIN lens (recording examples shown in Fig. 3e).

To compare neural activity across methods, we analyzed population peristimulus time histograms (PSTHs), which revealed differential responses to go and no-go trials (Fig. 3f). In line with that, we found several touch-modulated units that selectively responded to either one of the two aperture stimuli (Fig. 3g). Touch-modulated units comprised 63.2% in the BC (261 out of 413 units, with 142 responsive to the wide aperture, 28 to the narrow aperture, and 91

to both), 46.7% in the VPM (196 out of 420 units, with 90 responsive to the wide aperture, 53 to the narrow aperture, and 53 to both), 49.4% in the POm (129 out of 261 units, with 70 responsive to the wide aperture, 23 to the narrow aperture, and 36 to both), and 45.6% in the ZIv (67 out of 147 units, with 23 responsive to the wide aperture, 9 to the narrow aperture, and 35 to both). Compared to the electrophysiology results, we found a similar proportion of touch-modulated units in the calcium imaging data of POm (48.2 %, 78 out of 162 units), with 34 responsive to the wide aperture, 31 to the narrow aperture, and 13 to both.

Furthermore, a convolutional neural network was trained to classify calcium transients over the whisker-aperture contacts (see Methods). The classifier could reliably distinguish the aperture width based on the neural calcium transients with the validation accuracy of 87.65% (Fig. S3b, c).

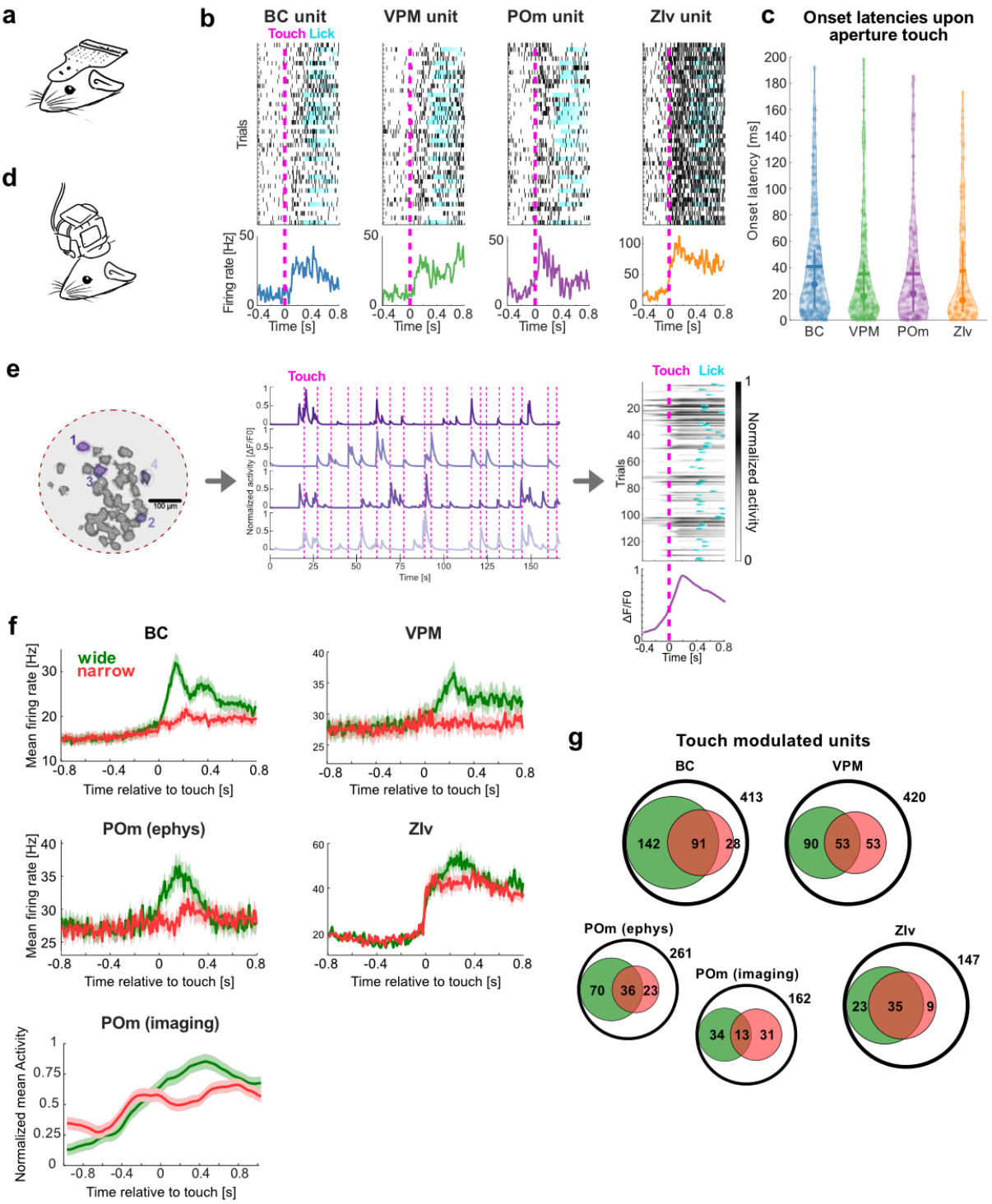
a
b
BC unit
VPM unit
POm unit
Zlv unit
Touch Lick
Trials
Firing rate [Hz]
Time [s]
c
Onset latencies upon aperture touch
Onset latency [ms]
BC
VPM
POm
Zlv
d
e
Touch
Normalized activity [ΔF/F0]
Touch Lick
Trials
Normalized activity
ΔF/F0
f
BC
VPM
wide
narrow
Mean firing rate [Hz]
Time relative to touch [s]
POm (ephys)
Zlv
POm (imaging)
Normalized mean Activity
g
Touch modulated units
BC
413
142
91
28
VPM
420
90
53
53
POm (ephys)
261
70
36
23
POm (imaging)
162
34
13
31
Zlv
147
23
35
9

247

Fig. 3: Neural activity patterns during aperture discrimination task. **a:** Schematic representation of a head-mounted EIB. **b:** Representative raster plots of single unit spiking activity in BC, VPM, POm, and ZIv, aligned to the time of whisker-aperture contact (magenta line). Below each raster plot, corresponding PSTHs display mean firing rates. **c:** Onset latencies of neuronal responses following whisker contact with the aperture across different brain regions. Latencies were computed based on the first significant deviation from baseline activity (see Methods). Violin plots depict the distribution of response latencies, with mean values highlighted as bars, and median with IQR as filled circles with whiskers. **d:** Schematic representation of a head-mounted UCLA Miniscope V4. **e:** Spatial footprints of POm units from one example imaging session (left), with four touch-modulated units highlighted in color. Example normalized calcium transients (ΔF/F0) from the four touch-modulated POm units (middle), with magenta lines indicating whisker touches with the aperture. Trial-aligned calcium transients of a representative POm unit and averaged across trials below. Lick onsets are marked in blue. **f:** Population PSTHs displaying the mean firing rate (± SEM) of different brain areas, for wide (green) and narrow aperture trials (red), over all expert sessions. Neural activity is aligned to the time of whisker-aperture contact. For POm, normalized calcium activity (±SEM) from 39 POm neurons detected in a single session is shown. **g:** Venn diagrams showing proportions of touch-modulated units/neurons per brain region (from a total sample indicated by black circles). Units/neurons responding selectively to the wide aperture are shown in green, those responding to the narrow aperture in red. The intersection represents units responsive to both apertures.

Bilateral whisker input and barrel cortex are necessary for normal task performance and learning

Inspired by the popular texture-discrimination paradigm for rodents, our initial task design used sandpapers. However, we found that in our freely-moving configuration, mice exploited olfactory cues for sandpaper discrimination, evidenced by undisrupted performance when the whiskers were plucked or the sandpapers were reversed to the textureless backside. Subsequent NMDA lesions in the olfactory bulb completely abolished task performance (Fig. S4a), confirming that olfaction alone can drive discrimination in texture-based paradigms.

In contrast, the aperture-based task is purely whisker-dependent, as demonstrated by the following experiments. First, we performed bilateral whisker plucks in expert mice. The complete removal of whiskers, deteriorated the performance of expert animals below performance threshold (Fig. 4a). In contrast, animals continued to perform at expert level with IR backlights and IR overhead LEDs turned off, demonstrating that visual cues were not used to solve the task (Fig. S4b). These results show that by using apertures with variable widths, eliminates the unintended olfactory cues, ensuring that discrimination relies solely on whisker-mediated tactile processing.

To investigate the requirement of bilateral whisking we trained an additional cohort on 20 mm and 6 mm contrasts to expert-level performance, followed by unilateral whisker plucking. The performance dropped in all mice, however, only for the 6 mm contrast the performance dropped under the expert-level threshold (Fig 4b). Similarly, when removing one of the aperture wings on each side of the track, mean population performance dropped below the expert-level performance threshold even for 20 mm contrast (Fig. S4c). Together these results demonstrate that bilateral whisking is required for smaller contrasts but animals might be able to use other facial parts to discriminate bigger contrasts.

We next addressed whether the BC is required for normal task execution and task learning by ablating the BC bilaterally similar as in [19] (Fig. 4d Inset). Sham lesions served as control

cohorts. In the first experiment, we addressed the BC-dependency for task execution with BC ablations in expert animals (Fig. S4d). Ablated animals, but not sham controls dropped below the performance threshold, demonstrating that task execution is BC-dependent (Fig. 4c). In a second experiment, we performed BC ablations and sham operations in naive animals and trained them on the basic task rule. While sham controls showed normal learning times (~500 trials to reach expert level), the learning in BC-ablated animals was severely impaired, with a roughly four-fold increase in trials required for expert level performance (Fig. 4d). Furthermore, the performance of BC-ablated animals remained marginally above expert-level performance and never reached similar d' levels as sham animals (Fig. 4e), as reflected by the larger proportion of trial-by-trial performance drops (Fig. S4e) and broader distribution of residuals from the sigmoidal fit (Fig. S4f).

Given these findings, we next sought to determine whether temporarily disrupting whisker input in expert mice would similarly impact performance. Therefore, we applied a local anesthetic (4% Lidocaine cream) to both whisker pads of expert mice. For control a neutral ointment was used. Performance dropped below the expert-level-performance threshold with lidocaine application (Fig. 4f). To determine whether this impairment was due to altered whisker kinematics, we used a Generalized Additive Model[31] classifier to decode aperture width from whisker angular trajectories (Fig. 4g for expert sessions). Decoding accuracy remained high in both lidocaine and control conditions and significantly exceeded chance level (Fig. 4h), suggesting that whisker motion itself was not disrupted by local anesthesia. Passive whisker deflection upon encountering the apertures of variable width (Fig. S4g for control sessions), likely contributed to the high decoding accuracy. However, when decoding aperture width from spike trains recorded across different brain areas, we observed a marked reduction in classification accuracy during lidocaine sessions compared to controls (Fig. 4i), demonstrating that sensory information processing was impaired at the neural level.

Together, these results show that both learning and task execution of the freely moving discrimination paradigm are dependent on intact whiskers and the BC.

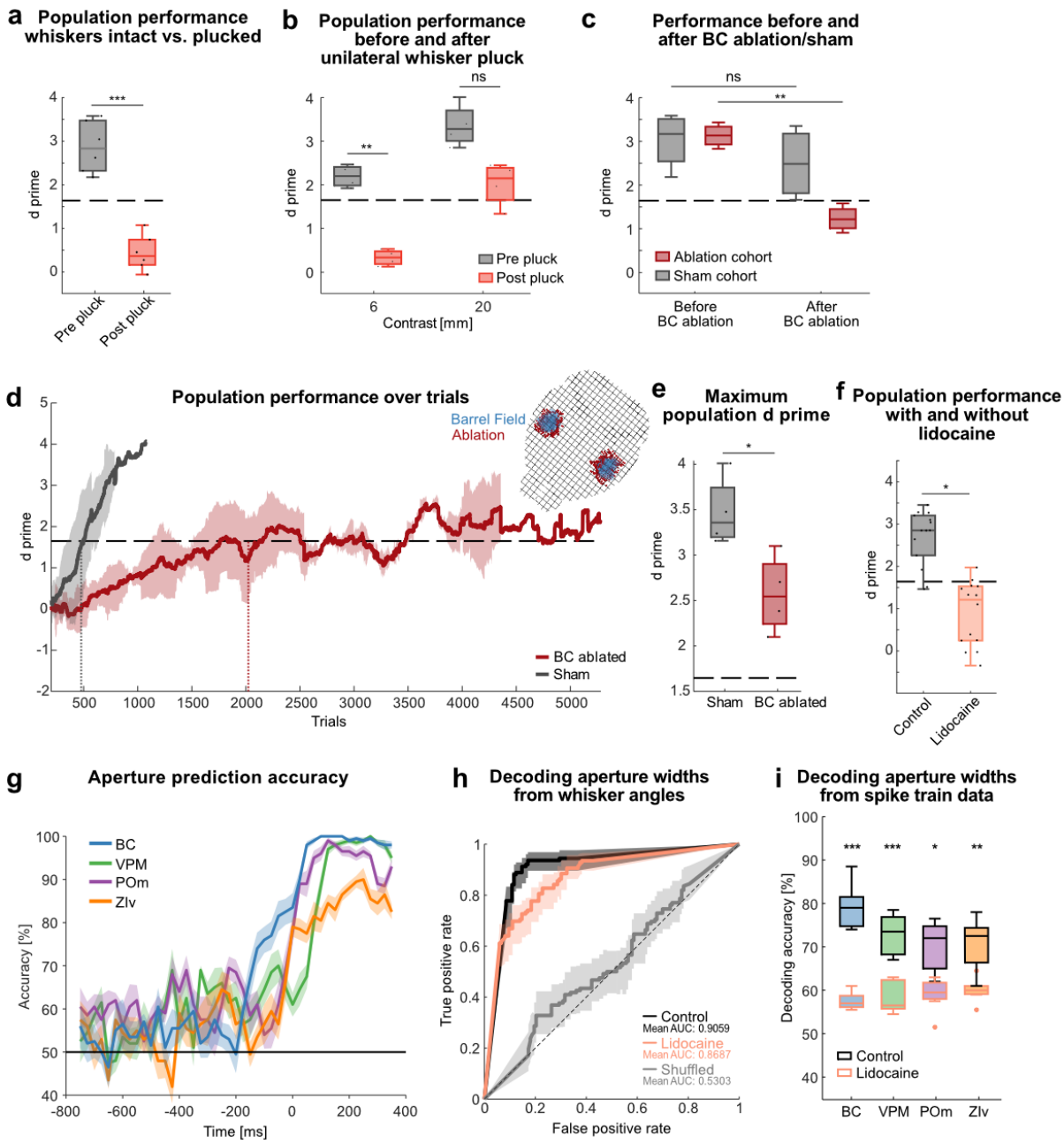

Fig. 4: Intact whisker input and barrel cortex are necessary for normal task performance and learning. **a:** Population performance for expert animals before and after bilateral whisker-pluck. Performance calculated from last session before and first session after the whisker pluck, each dot represents one session, dashed line indicates expert-level threshold (d' = 1.65), n = 6 mice. **b:** Same as in a but with unilateral whisker pluck and for contrasts of 6 and 20 mm (n = 4 mice for each contrast). **c:** Same as in a but with barrel cortex ablations (red) or sham operations (grey). **d:** Performance over trials in barrel cortex ablated mice (red) and sham operated animals (grey). Expert-level performance (d' = 1.65, grey horizontal dashed line) was crossed after 478 vs. 2023 trials for sham (grey vertical dashed line) and ablated mice (red vertical dashed line), each n= 4 mice. Inset: example reconstruction of barrel cortex ablation. **e:** Population performance for expert animals in d, calculated from the session with the maximum d prime for each mouse (n = 4 mice each). **f:** Population performance for expert animals (n = 4 mice) with alternating application of lidocaine or neutral ointment (control) to the whisker pad. Performance was calculated from 7 lidocaine and 7 control sessions across all mice for each condition. Same conventions as in a. **g:** Time-resolved decoding accuracy of aperture width from spike data of different brain areas. Spike data was analyzed from expert sessions (800 ms before to 400 ms after

aperture touch). **h:** Receiver operating characteristic curves from a generalized additive model classifier based on whisker angles after whisker-touch onset. Comparison of control (black), lidocaine sessions (orange), and randomly shuffled labels (light gray). Accuracies for control and lidocaine sessions were not significantly different from each other, but both differed significantly from the shuffled accuracies (n = 3 mice). **i**: Decoding accuracy from spike data for lidocaine sessions (orange boxes) and control sessions (black boxes). The mean decoding accuracy was calculated over a time window from trigger onset to 400 ms post-trigger onset (see Methods). Number of units (from n = 3 mice) in lidocaine sessions: 128 (BC), 100 (VPM), 52 (POm), 17 (ZIv); and control sessions: 150 (BC), 101 (VPM), 64 (POm), 17 (ZIv).

ns: $p > 0.05$, *: $p \leq 0.05$, **: $p \leq 0.01$ and ***: $p \leq 0.001$; **a, b:** two-tailed paired t-test, **c:** two-way anova, **e:** independent samples t-test, **f:** repeated measures anova, **i:** two-tailed Wilcoxon rank sum test. For exact statistics see Supplementary Table 1.

Capturing naturalistic decision-making, active touch strategies, and dynamic behavioral states during learning

In head-fixed go/no-go paradigms, licking is the primary decision variable. However, in our freely moving paradigm, an earlier decision-revealing movement—the mouse's approach or withdrawal from the aperture—may provide additional insights into decisions and learning. Indeed, during CR trials, mice exhibited a turning behavior, which we used to estimate reaction time (time between aperture touch and turning) and reaction distance (how close the mouse approached the LP before turning). Both measures closely correlated with performance: expert mice showed significantly shorter reaction times and distances, indicating a refined and more efficient decision-making process (Fig. 5a-c).

Moreover, we observed a refinement of licking behavior. While naive mice exhibited comparably late and more variable lick latencies following whisker-aperture interaction, expert mice showed earlier and more reliable licks (Fig. 5d for a representative session). Population analyses confirmed this trend, showing a systematic decrease in lick latencies and variability with learning (Fig. 5e).

To assess active touch strategies, we analyzed whisker kinematics and their relationship to aperture contact events. Whisker tracking revealed a rhythmic pattern of whisking at 14.5 ± 3.1 Hz (mean ± std) (Fig. 5f), consistent with previously described whisking frequencies in freely moving mice[32]. Interestingly, while the number of whisking cycles remained stable in FA trials, they significantly decreased in CR trials as mice became experts (Fig. 5g).

Heat maps of positional data illustrate that mice preferentially occupied the sampling and reward areas, while avoiding exposed regions (Fig. 5h). This pattern may reflect a strategic balance between exploration and risk avoidance. Analysis of spatial tuning revealed a subset of putative spatially tuned units that exhibited distinct firing rate modulations in relation to position on the track (Fig. 5i), with significant proportions of such units found across multiple brain regions (2.4±2.1% in BC, 6.2±4.3% in VPM, 8.7±3.9% in POm, 11.5±12.7% in ZIv; Fig. 5j).

We also found neuronal activity to be modulated by locomotor state. Comparing firing rates during rest and locomotion revealed a subset of units with locomotion-enhanced or

locomotion-suppressed activity (Fig. 5k). Notably, significant increases in mean firing rates during movement were observed in VPM, POm, and ZIv on a population level.

In summary, the tactile discrimination paradigm can be utilized to study different motor behaviors over the course of tactile discrimination learning. The results demonstrate that learning manifests itself not only in increased tactile discrimination performance but also in an adaptation of motor behaviors.

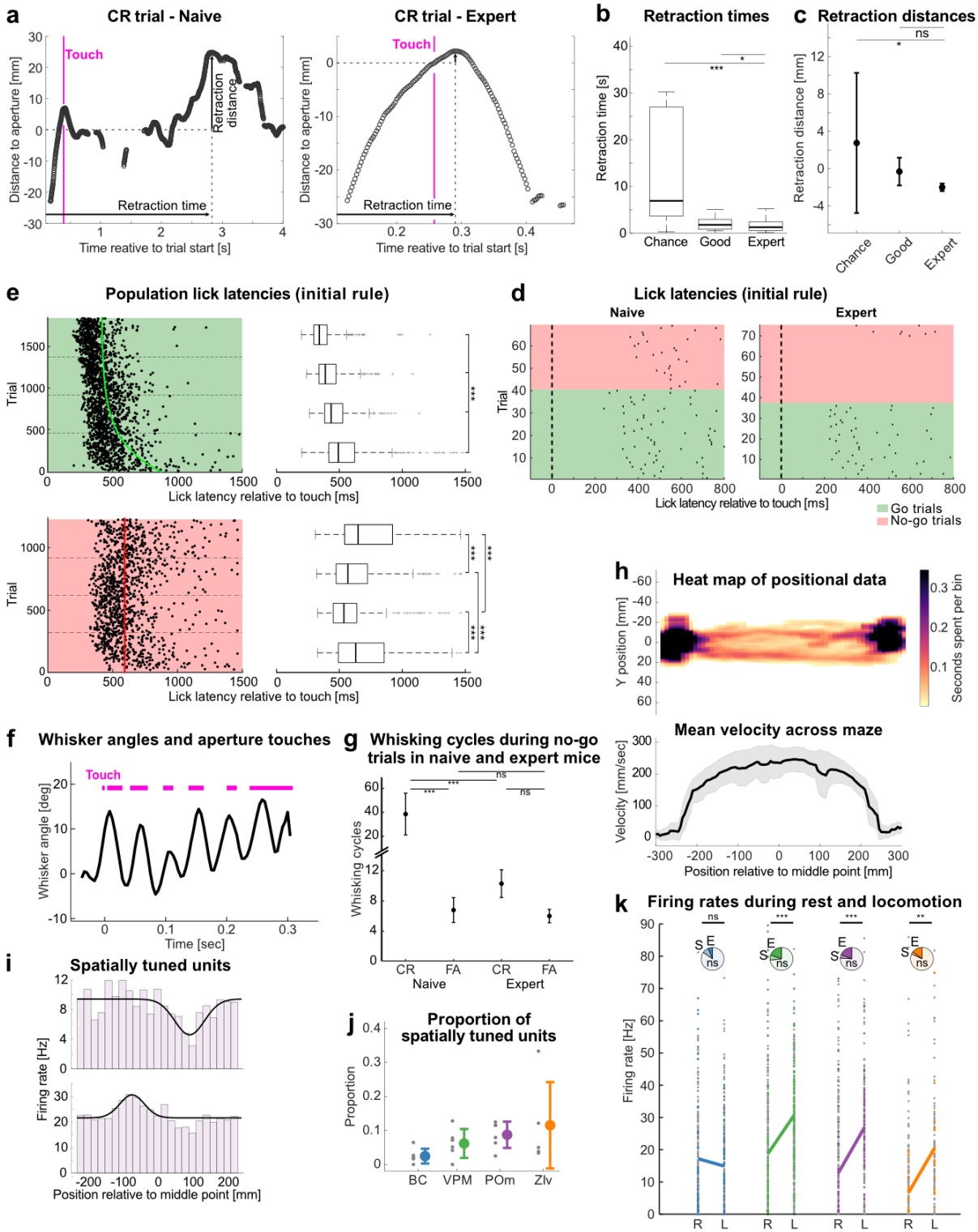

Fig. 5: Capturing naturalistic decision-making, active touch strategies, and dynamic behavioral states during learning. **a:** Approaching behavior to the lick spout following whisker contact ("Touch") with the aperture in a CR trial, shown for a naive session (left) and an expert session (right). The blue trace represents the snout trajectory over time. Retraction time and distance are quantified from the maximum of the trajectory (= turning point), with respect to the beam break (retraction time) and aperture position (retraction distance). **b:** Retraction times across different learning stages (chance, good, expert). **c:** Same as b for Retraction distances (mean with 95%CI). **d:** Example lick latencies from one mouse after whisker-aperture interaction (t = 0 ms) for an early (naive, left) and an expert session (right). Go trials are highlighted in green, no-go trials in red. **e:** Population lick latencies (n = 6 mice) following whisker-

aperture interaction (t = 0ms) across the initial learning stage for Hit (green) and FA (red) trials. Trials are grouped into four equal bins based on trial progression for statistical comparison between early (bottom) and late (top) trials. Trendlines (green and red) represent the best-fit asymptotic function (see methods). **f:** Example whisker angle and aperture touches (magenta) during a hit trial (averaged angle values α from four DeepLabCut-tracked whiskers). **g:** Number of whisking cycles during CR and FA trials (mean with 95%CI) in naive (initial 4 sessions) and expert sessions (final 4 sessions). **h:** Heat map of positional data along the linear track of the setup of an exemplary session. The color indicates the time spent in that area (see Methods). The corresponding mean velocity across the track is shown below. **i:** Representative examples of spatially tuned units, showing firing rates as a function of position relative to the middle point (mm), with firing rate histograms and fitted gaussian tuning curves (black). **j:** Proportion of spatially tuned units across all recorded brain regions. Each dot represents the mean proportion for an individual animal, with the cohort mean ± standard deviation as colored bars. **k:** Firing rates during rest (R) and locomotion (L), across brain regions. Each dot represents the firing rate of a single unit (non-significant units in grey, significant units in color). Pie charts indicate the proportion of significantly modulated units (E: enhanced activity; S: suppressed activity). Solid lines connect mean firing rates during R and L for significantly modulated units.

ns: $p > 0.05$, *: $p \leq 0.05$, **: $p \leq 0.01$ and ***: $p \leq 0.001$; **b, c, g:** two-tailed Wilcoxon rank sum test, **e:** Kruskal-Wallis Test, **k:** two-tailed paired t-test; n = 413 (BC), 420 (VPM), 261 (POm), and 147 (ZIv) units in total. Data was pooled from n = 6 mice. For exact statistics see Supplementary Table 1.

Neural encoding of whisker- and head kinematics during active sensory exploration

To investigate the relationship between whisker kinematics and neural representations during task execution, we analyzed the modulation of firing rates by whisking parameters, including whisker angle and whisking phase. We observed a significant increase in mean firing rates during whisking compared to quiescence across all recorded brain regions (Fig. S5), emphasizing the neural engagement during active sensory exploration. We further identified a subset of roughly 10% of units (10.5±2.2% in BC, 9.8±10.6% in VPM, 10.8±8.4% in POm, 12.4±6.3% in ZIv) across all four recorded brain regions—BC, VPM, POm, and ZIv—that exhibited significant modulation by whisking angle (Fig. 6a,b), as determined by comparisons to null distributions (see Methods). The proportions of these whisker angle-tuned units were comparable between VPM and POm, consistent with previous reports in both head-fixed awake[27] and freely moving mice[33]. Further examination of whisking phase tuning showed distinct subsets of units in each area (33.2±11.5% in BC, 39.3±15.0% in VPM, 34.0±10.0% in POm, 31.1±16.3% in ZIv) that were modulated by the phase of the whisking cycle (Fig. 6c,d). Analysis of population polar plots revealed a preference for protraction states among phase-tuned units (143.5° in BC, 176.8° in VPM, 179.8° in POm, 157.6° in ZIv; Fig. 6e), suggesting that neural representations of whisking dynamics are temporally structured and phase-dependent.

Beyond whisker-based encoding, we examined whether neural populations also track head kinematics. We found that BC, VPM, POm, and ZIv carry information about head azimuth (Fig. 6f), in agreement with the recent observation of head-movement coding in POm and VPM[33]. Notably, while the overall proportion of head-angle tuned units was comparable across regions (Supplementary table 1), ZIv exhibited a lower proportion of allocentric head-tuned units, though this difference was not statistically significant (p (ZIv vs. BC) = 0.0625; p (ZIv vs. VPM) = 0.4375; p (ZIv vs. POm) = 0.3125, two-sided Wilcoxon signed rank test, Fig. 6f).

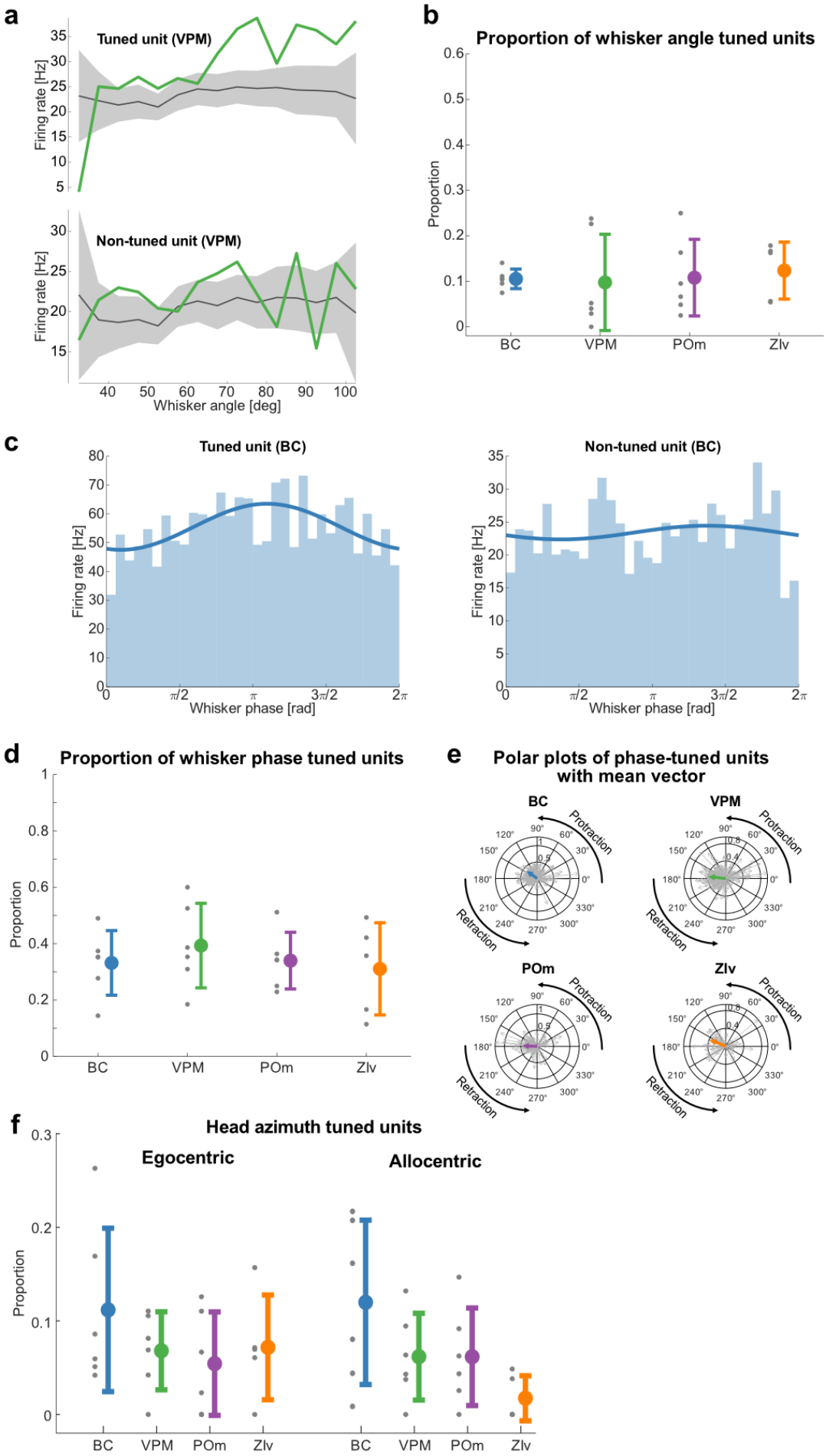
a
Tuned unit (VPM)
Non-tuned unit (VPM)
Firing rate [Hz]
Whisker angle [deg]
b
Proportion of whisker angle tuned units
Proportion
BC
VPM
POm
Zlv
c
Tuned unit (BC)
Non-tuned unit (BC)
Firing rate [Hz]
Whisker phase [rad]
d
Proportion of whisker phase tuned units
Proportion
BC
VPM
POm
Zlv
e
Polar plots of phase-tuned units with mean vector
BC
VPM
POm
Zlv
Protraction
Retraction
f
Head azimuth tuned units
Egocentric
Allocentric
Proportion
BC
VPM
POm
Zlv

Fig. 6: Neural encoding of whisker- and head kinematics during active sensory exploration. **a:** Representative examples of whisker angle tuning in the VPM, showing firing rates of a tuned unit (top) and non-tuned unit (bottom) as a function of whisker angle with null distributions (grey, mean ± SEM). **b:** Proportion of units significantly tuned to whisker angle in the BC, VPM, POm, and ZIv (see Methods). Each dot represents the mean proportion for an individual animal, with the cohort mean ± standard deviation as colored bars. **c:** Examples of whisker phase tuning in the BC, with firing rates plotted for a tuned unit (left) and a non-tuned unit (right) across whisker phases. A sinusoidal function is fitted to the respective distribution. **d:** Proportion of units significantly tuned to whisker phase in the BC, VPM, POm, and ZIv. Representations follow the logic of Fig. 6b. **e:** Polar plots of phase-tuned units across brain regions, displaying individual vectors (grey arrows) and the mean population vector (colored arrows) of whisker phase tuning. **f:** Proportion of units tuned to head azimuth with egocentric (left) and allocentric (right) references across BC, VPM, POm, and ZIv. Representations follow the logic of Fig. 6b.

a: Test against null-distribution of shuffled spike times (see Methods), **c:** Kuiper test; n = 413 (BC), 420 (VPM), 261 (POm), and 147 (ZIv) units in total. Data pooled from n = 6 mice.

Discussion

This study introduces a go/no-go whisker-dependent discrimination paradigm for freely moving mice. Compared to head-fixed paradigms, this novel paradigm enables investigations into mouse behavior and learning in a more natural and unrestrained environment, while being compatible with high-resolution electrophysiology, imaging and motor behavior measurements. This unrestrained configuration offers richer readouts of naturalistic behaviors. For instance, head movements, which are absent in restrained configurations, can be used as a decision readout, in addition to commonly used lick analysis. Another benefit of the unrestrained paradigm is the clear temporal separation between sensory sampling and reward consumption, which reduces confounding influences of lick-related activity during perception. In head-fixed paradigms, anticipatory licking often overlaps with sensory processing, making it difficult to distinguish sensory-evoked activity from licking-related neural responses. Our task design mitigates this issue by ensuring that licking occurs only after a perceptual decision is made. The discrimination task relies solely on somatosensory whisker information for aperture discrimination, demonstrated by deteriorated performance when whiskers were anesthetized or removed. Furthermore, compared to texture discrimination tasks [6,17,34–37], in which surface differences are created by switching between different sandpapers, the use of the same apertures with variable widths ensures the elimination of potential confounders from olfactory cues.

Learning speeds and discrimination performance were stereotypical between mice, with fast learning within a total training time of approximately four hours, spread over eight days (two 15-minute sessions per day). This fast learning not only allows for high-throughput behavioral analysis but also provides several other advantages. First, the paradigm allows the incorporation of multiple consecutive learning stages in which mice learn different rules (initial, neutral, reversal, devaluation, within a total of 29 ± 4 days). Second, the paradigm can be used in repeated rule switch mode, by switching back and forth between two inverted rule sets (Fig. 2d). This can be advantageous for learning studies that require a steady-state learning environment without confounding learning factors which happen only in the initial learning when mice are exposed to the learning paradigm for the first time. Indeed, we found several behavioral adaptations which happen in the initial learning and then stabilize, for example overall activity (trial counts per session), lick latencies, and overall learning speed, which progressively approached an efficient optimum following multiple rule switches. Most

importantly, the fast learning allows for chronic neurophysiology within a short experimental time frame. This is advantageous to monitor neuronal activity over the entire learning period and even during multiple learning rules, which is often difficult to achieve because of the deteriorating signal quality and unit yield in chronic electrophysiological and optical recordings [38–40].

During early learning and extinction phases, mice initially engaged in constitutive licking across all trials, regardless of aperture width. This behavior, which resulted in a 50% reward/punishment rate, suggests that the motivational value of the reward outweighed the negative impact of punishment when the sensory cues were not yet predictive. Mice flexibly adapted to changing rules, demonstrating behavioral updating when the predictive relationship between sensory cues and outcomes changed. Our results further indicate a faster relearning of previously learned rules (Fig. S1g), a phenomenon known as "savings" from human studies [41,42].

Mice reliably discriminated between different aperture widths, with a discrimination threshold of approximately 6 mm – comparable with rats in a forced-choice setting (smallest discriminable contrast of 3 mm [20]). However, given sufficient motivation, mice likely achieve even finer discrimination, as they have been shown to detect submillimeter differences in sandpaper textures [35]. In contrast to texture discrimination tasks, where the whiskers interact with fine surface features via stick-slip micromotions [37,43–45] our distance discrimination task likely depends more on whisker-angle changes.

Furthermore, we find that both, bilateral whisker input and barrel cortex, are necessary for normal task performance and learning. This is in agreement with cortex-dependency for whisker discrimination tasks reported earlier [36].

Electrophysiological and optical recordings revealed touch-modulated single unit responses in multiple brain regions, including the BC, VPM, POm, and ZIv. Using the spike-trains or calcium transients allowed for accurate decoding of the aperture width while Lidocaine numbing of the whisker pad significantly impaired decoding from spike trains. Together this demonstrates that task-relevant information for tactile discrimination is encoded in the thalamocortical system in addition to several movement and sensory variables. More specifically, we find that neuronal activity is tuned to locomotion (Fig. 5k), whisking (Fig. S5), whisker angle (Fig. 6a, b), whisker phase (Fig. 6c-e), head angle (Fig. 6f), and spatial position (Fig. 5i, j). Characterizing movement- and stimulus-related tuning in a freely moving paradigm, provides an opportunity to investigate how sensorimotor integration contributes to perceptual decision-making in a more naturalistic setting. While further studies are needed to fully elucidate the underlying mechanisms, these analyses establish an important foundation for understanding how different neural circuits coordinate movement and sensory processing to guide behavior.

535 **Material & Methods**

Product	Supplier
Linear track (82 x 10 cm, wood)	Custom built, Lee Embray, Heidelberg
Controlling unit of the behavioral apparatus (Arduino Uno R3 with firmata firmware)	Arduino, assembled by Lee Embray, Heidelberg
Apertures	
Metal wings (height: 205 mm, width: 97 mm, aluminum)	Lee Embray, Heidelberg
Controlling unit with stepper motors (https://github.com/GrohLab/A-tactile-discrimination-task-to-study-neuronal-dynamics-in-freely-moving-mice/blob/main/MaterialList/ApertureGate/info.md) [24]	Lee Embray, Heidelberg
Lick ports adapted from Cornelius Schwarz, Tübingen [46]	
Vasofix® Safety Braunüle® FEP G16	B. Braun SE, Melsungen, Germany
Piezo sensor (#285-784)	RS components GmbH, Mörfelden-Walldorf, Germany
Analog-to-digital converter (ADC)	Cornelius Schwarz, Tübingen [46]
Sensors and IR illumination	
Light beams (https://github.com/GrohLab/A-tactile-discrimination-task-to-study-neuronal-dynamics-in-freely-moving-mice/blob/main/MaterialList/LightBeams/info.md) [24]	Lee Embray, Heidelberg
LED strips for overhead illumination (Synergy 21 LED Flex Strip infrarot IR 12 12V IP65 Security Line 850nm, #140455)	ALLNET GmbH, Germering, Germany
Backlight LEDs (HT-110IRPJ IR-Emitter 850 nm 140° 1204 SMD)	Harvatek Corporation, Hsinchu, Taiwan
Diffuser plate (3D printed with clear FLGPCL04 and sanded with P600)	Formlabs GmbH, Berlin, Germany
Diffuser film, 60% light diffusion (#DSF-10)	Folien Fischer UG, Hamburg, Germany
Intervention drugs	
Isoflurane (Isofluran Baxter)	Baxter Deutschland GmbH, Germany
Buprenorphine (Bupresol vet. Multidose 0,3 mg/ml, 10 ml)	CP-Pharma Handelsgesellschaft mbH, Burgdorf, Germany
Ketamine (100 mg/ml, 10 ml)	CP-Pharma Handelsgesellschaft mbH, Burgdorf, Germany
Xylazine (Xylavet® 20 mg/ml)	CP-Pharma Handelsgesellschaft mbH, Burgdorf, Germany
Lidocaine (Xylocaine® 1%)	Aspen Pharma Trading Limited, Ireland

ssAAV-1/2-hSyn1-chI-GCaMP6f-WPRE-SV40p(A)	Viral Vector Facility (VVF), Zürich, Switzerland
N-Methyl-D-aspartic acid, 98% (#AC329190500)	Thermo Fisher Scientific Inc., MA, USA
Cameras	
2x High speed cameras (DMK 37BUX287)	The Imaging Source Europe GmbH, Bremen, Germany
Overview camera (DMK 37BUX290)	The Imaging Source Europe GmbH, Bremen, Germany
Reward / punishment	
Food dispensers (https://github.com/GrohLab/A-tactile-discrimination-task-to-study-neuronal-dynamics-in-freely-moving-mice/blob/main/MaterialList/FoodDispensers/info.md) [24]	Lee Embray, Heidelberg
2 ml syringes (BD Discardit II)	Becton Dickinson GmbH, Heidelberg, Germany
Tubes with Luer connector (#4256000)	B. Braun SE, Melsungen, Germany
Hifi integrated amplifier (A-S301)	Yamaha Music Europe GmbH, Rellingen, Germany
2x Speakers (Neo X 3.0 ribbon tweeter)	Fountek Electronics Co., Ltd, Zhejiang, China
EIB	
RHD USB Interface Board (#C3100)	Intan Technologies, CA, USA
Samtec Male Connector EIB (ST4-40-1.00-L-D-P-TR)	Samtec Europe GmbH, Germering, Germany
Samtec Female Connector Headstage (SS4-40-3.00-L-D-K-TR)	Samtec Europe GmbH, Germering, Germany
PCB (EIB and headstage)	Custom built (BRD file: https://github.com/GrohLab/A-tactile-discrimination-task-to-study-neuronal-dynamics-in-freely-moving-mice/blob/main/MaterialList/EIB64-ST4-Multi.brd) [24], printed by Multi-Circuit-Boards Ltd, Munich, Germany
Tungsten 99.95% CS Wire for Tetrodes (#100211)	California Fine Wire Company, CA, USA
Gold chloride solution for gold plating (200 mg/dL gold chloride in deionized water, HT1004-100ML)	Sigma-Aldrich, Inc., MO, USA
Intan Interface 64 Channel Amplifier Chip (RHD2164)	Intan Technologies, CA, USA
UV-curable adhesive (3M™ Filtek™ Supreme XTE)	3M Deutschland GmbH, Neuss, Germany
Function generator (A365 Stimulus Isolator)	World Precision Instruments, Inc., FL, USA
Electric Rotary Joint (AHRJ-OE_2x2_AD_200-0.22_24_USB-C)	Doric Lenses Inc., Quebec City, Canada
Miniscope V4	

Miniscope V4 main body (Excitation, objective, and emission module)	Custom print from Heidelberg precision mechanics workshop/ Open Ephys
V4 Base Plate	Custom print from Heidelberg precision mechanics workshop/ Open-Ephys
Rigid-Flex PCB	Open-Ephys
Optical Filters - Excitation filter 4mm x 4mm, ET47/40x - Emission filter 4mm x 4mm, ET525/50m - Dichroic mirror 6mm x 4mm, T495lpxr	Chroma/ Open-Ephys
Lenses - 2 x 3mm diameter, 6mm FL achromat used in the objective module (#45-089) - 4mm diameter, 10mm FL achromat used in the emission module (#63-691) - Half-ball Lens, 3.0mm Diameter, N-BK7 (#47-269)	Edmund Optics/ Open-Ephys
Coax cable, 36AWG 26/50SPC	Cooner Wire
Hirose U.FL Connector, U.FL-PR-SMT2.5-1(10)	Mouser
GRIN Lenses, ProView™ Lens Probe, 0.5mm diameter, ~4.0mm length	Inscopix

Table 1: Parts list

Ethics Statement

All experimental procedures were approved by the local governing body (Regierungspräsidium Karlsruhe, Germany, approval numbers: 35-9185.81/G-216/19 and 35-9185.82/A-8/20) and performed according to their ethical guidelines.

Animals

The experiments were done with adult male mice from the inbred strain C57BL/6NRj (Janvier Labs, Le Genest-Saint-Isle, France). Mice were 8-10 weeks old at the start of training, with a mean body weight of 25.94 ± 2.33 g (mean ± standard deviation) at the start of the experiments. Mice were separately housed in a ventilated Scantainer (Scantainer Classic, SCANBUR A/S, Karlslunde, Denmark) under a 12-hour inverted light/dark cycle (lights off at 7:00 a.m. and on at 7:00 p.m.) at a controlled temperature (20-24 °C) and humidity (45-65 %). During behavioral training, mice were held on a controlled food intake schedule, and their body weight was maintained at 95-85% of their initial body weight. Under the controlled food intake schedule, mice were given dry food pellets (10-20 % of their body weight) daily at the end of behavioral training. Water was available ad libitum.

Behavioral apparatus

Behavioral testing and recording were conducted on an elevated, dark-toned linear platform measuring 82 cm in length and 10 cm in width (technical drawings are available on https://github.com/GrohLab/A-tactile-discrimination-task-to-study-neuronal-dynamics-in-freely-moving-mice/tree/main/MaterialList) [24], featuring a lick port (LP) at both ends. To access the LPs, mice were required to traverse through an aperture between two aluminum wings mounted onto a motor to adjust the distance between the wings (= aperture width) in each trial. Each LP consisted of a cannula attached to a syringe filled with condensed milk. A piezo sensor, mounted on top of the cannula, detected vibrations and registered lick events. A

speaker was mounted close to the LP to deliver white noise. A lick event resulted in either reward delivery (10 µl of condensed milk) or punishment (120 dB white noise, random duration between 1 and 3 seconds) (Fig. 1B). Moreover, three pairs of infrared (IR) sensors were placed along the track, one in the center of the track and the other two in front of the apertures. Three cameras were positioned above the setup: an overview camera (60 Hz frame rate), providing a view of the entire platform, and two high-speed cameras (240 Hz frame rate) capturing the aperture and LPs for later analysis of whisker movements and touch events (Fig. 1A, Suppl. Videos 1-3). The behavioral apparatus was controlled using Syntalos (Code available at https://github.com/syntalos/syntalos), which controlled the devices and recorded the timing of events (i.e., aperture state, reward/punishment administration, lick detection, and beam crossings of the mice), cameras, electrophysiology, and miniscope signals.

Behavioral paradigm

Mice were trained to perform a go/no-go whisker-dependent paradigm on a linear track (Fig. 1), in which they had to learn to discriminate between apertures of different widths to get a reward and avoid punishment. Mice had to choose the correct response depending on the presented stimulus. The response can either be a lick response (hit for go trials, false alarm [FA] for no-go trials respectively) or to refrain from licking (crossing of middle beam brake) and move on to the subsequent trial (miss for go trials, correct rejection [CR] for no-go trials respectively). Animals were trained on the setup twice per day, each training session lasting 15 minutes, with a break of at least two hours between the two sessions. At the beginning of the session, the mouse was put on the setup at the middle IR beam (Fig. 1A) to start the session. The mouse then runs to one end of the linear track. A trial started when one of the outer IR beams was crossed (Fig. 1A) during the approach to the aperture. Upon sampling the aperture with its whiskers, the mouse has to decide to either lick at the LP or turn and go to the other side of the linear track. A trial ends either after a lick response or, in case the mouse didn't lick, when the mouse crosses the middle point on its way to the other LP. At the beginning of each trial (crossing one of the outer IR beams), the aperture state on the opposite side end of the track was reset randomly. The apertures also perform mock movements when the same aperture was presented twice in a row to avoid any learning due to auditory cues. Table 2 summarizes the stimulus-outcome rules for the different training stages.

Training procedure

The training procedure consisted of several stages, and mice must reach a predetermined criterion in each stage to move on to the next stage (Table 2). <u>Controlled food intake, handling, and LP training:</u> One week prior to behavioral training, the mice went onto a controlled food intake schedule while being handled and trained with the LP. During LP training, a dummy LP was placed in the mouse's home cage, which mimicked the appearance and functionality of the actual LP used in experimental tasks. Whenever the mouse approached the LP to lick, the experimenter manually dispensed condensed milk, as positive reinforcement to associate licking with receiving a reward. <u>Habituation stage:</u> Milk rewards were presented upon licking alternatingly at each LP in order to encourage mice to run back and forth between the two LPs. Apertures remain in the wide position. Once the mice reached criterion (Table 2), they progressed to the initial rule stage. <u>Initial rule stage:</u> Go (45 mm "wide") and no-go (25 mm "narrow") apertures were presented with an equal probability of 50 % in a random sequence. Licking upon the go (wide) aperture triggered a reward, and licking at the no-go aperture triggered a punishment (Table 2). Individual mice completed the initial rule stage at an individual point in time, defined by the

expert-level criteria (Table 2). For the experiments that involved a gradual decrease in aperture contrast (Fig. 3A), a new aperture width was introduced once the mouse reached the expert-level criterion or when the mouse performed ≥ 4 sessions and ≥ 500 trials at a performance level below expert-performance threshold (d' = 1.65). The contrast was reduced to a minimum of 2 mm.

Neutral aperture stage: Reward and punishment contingencies remained as in the initial rule stage, but an additional "neutral" aperture (35 mm) was added. Licking upon the neutral aperture resulted in no outcome and no scoring. The neutral aperture stage lasted for 8 sessions (Table 2).

Reversed rule stage: Reward and punishment contingencies were inverted (i.e., the previously rewarded aperture was punished, and vice versa). The neutral aperture was not presented. Individual mice completed the reversed rule stage at an individual point in time, defined by the same expert-level criteria as in the initial rule stage (Table 2).

Extinction stage: Reward and punishment were randomly presented, irrespective of the aperture state. The extinction stage lasted for 8 sessions (Table 2).

Stage name	**Stimulus**	**Response**	**Scoring (outcome)**	**Criterion**
Habituation	45 mm aperture	Lick	Hit (reward)	≥ 4 sessions and ≥ 50 successful lick trials
		No lick	Miss (no outcome)	
Initial rule	45 mm aperture	Lick	Hit (reward)	≥ 4 sessions and ≥ 200 trials above expert-performance threshold (d' = 1.65)
		No lick	Miss (no outcome)	
	25 mm aperture	Lick	FA (punishment)	
		No lick	CR (no outcome)	
Neutral aperture stage	45 mm aperture	Lick	Hit (reward)	8 sessions in total
		No lick	Miss (no outcome)	
	35 mm aperture	Lick	No score (no outcome)	
		No lick	No score (no outcome)	
	25 mm aperture	Lick	FA (punishment)	
		No lick	CR (no outcome)	
Reversed rule	45 mm aperture	Lick	FA (punishment)	

		No lick	CR (no outcome)	≥ 4 sessions and ≥ 200 trials above expert-performance threshold (d' = 1.65)
	25 mm aperture	Lick	Hit (reward)	
		No lick	Miss (no outcome)	
Extinction	45 mm aperture	Lick	No score (random presentation of reward and punishment)	8 sessions in total
		No lick		
	25 mm aperture	Lick		
		No lick		

Table 2: Behavioral paradigm: training stages, stimuli, responses, scoring, outcomes and progression criteria. FA: false alarm; CR: correct rejection.

Data acquisition

Data acquisition during behavior was done with Syntalos [22]. An intan-module recorded all analog signals from the LPs. The overview camera was connected to a recorder module that operated continuously throughout the session. The high-speed cameras and an event list were controlled by a custom-made Python script. The cameras were programmed to start recording when the animal approached the corresponding LP, determined by the crossing of the corresponding light beam. The event list kept track of the triggered light beams and reported the state of the apertures. The list also noted if a trial was a success or failure.

Sensory deprivation protocols (whisker plucking and lidocaine numbing of the whisker pad)

For whisker plucking, mice were anesthetized with 2.5 % isoflurane and then placed in a stereotaxic alignment system (Kopf Instruments) with a mask providing continuous inhalation of 1-2 % isoflurane in medical oxygen. The body temperature was monitored and maintained at 37-39 °C. The mouse's head was tilted to see the whisker pad clearly under the microscope, and lidocaine cream was applied to the whisker pad. The whiskers were then plucked one by one using small cosmetic tweezers. After plucking all the whiskers (on both sides), mice were kept on a heating plate in their preheated cage for a minimum of 30 minutes to recover, and they were given at least 5 hours of rest before their next training session. In a separate sensory deprivation protocol, lidocaine cream was applied topically to the whisker pads during a brief anesthesia with isoflurane approximately 20-30 minutes in advance of the session. For control, neutral ointment (Bepanthen cream) was administered identically. The whiskers remained intact for this intervention.

Barrel cortex lesions

Mice were anesthetized with 2.5 % isoflurane and then placed in a stereotaxic alignment system (Kopf Instruments) with a mask providing continuous inhalation of 1-2 % isoflurane in medical oxygen. Carprofen (CP-Pharma) was given subcutaneously at a dose of 5 mg/kg, while lidocaine (Xylocaine 1%, Aspen Pharma) was injected beneath the scalp and around

the ear bars for local anesthesia. To keep the eyes lubricated during the surgery, Bepanthen ointment (Bayer) was applied. Once tail- and toe-pinch reflexes were confirmed absent, a midline incision was made in the skin, and the periosteum and aponeurotic galea were excised to expose the reference points bregma and lambda. The head was then properly aligned with the stereotaxic frame. Craniotomies were performed using the previously mapped borders of the barrel cortex on the skull as anatomical landmarks to ensure complete exposure of the barrel cortex. Next, a fine glass pipette was carefully inserted to a depth of 1.4 mm at the edge of the craniotomy. It was then moved along the contour 4 to 5 times until the brain tissue began to detach. Finally, the tissue was pulled and excised using thin needle bevels, and the surgical excision was complete when the white matter was visible.

Olfactory bulb lesions

Surgical preparations were conducted the same way as in the barrel cortex lesion procedures. A Hamilton syringe (10 µl) was used to inject N-methyl-D-aspartate (NMDA, 20 µg/µl, 1 µl per injection site, Thermo Fisher Scientific Inc., MA, USA) into the OB of the lesion group. Each hemisphere received injections at three sites (Table 3, coordinates relative to bregma). The needle was first lowered to the most ventral point of the injection, and NMDA was slowly delivered while retracting the syringe up to -0.3 mm below the dura, with a continuous injection rate of 100 nl/min. For control the same surgical procedure and injection protocol was followed, but with sterile saline solution replacing NMDA.

Site	**A/P**	**M/L**	**D/V with respect to dura**
1	**+5.25**	**+/-0.75**	**-1.5**
2	**+4.5**	**+/-0.75**	**-2.0**
3	**+3.75**	**+/-0.75**	**-2.5**

Table 3: Coordinates for OB lesion.

Electrophysiological recordings

Recording array

Electronic Interface Boards (EIBs) were based on the design developed in [47]. Tetrodes were manufactured in house by folding and twisting approximately 30 cm of tungsten wires (12.5 µm, Item # 100211, Tungsten 99.95% CS Wire, California Fine Wire Company). A total of 16 tetrodes (yielding 64 channels in total) were inserted to a custom-made EIB (produced by Multi-Circuit-Boards). The layout allowed for proper alignment of the tetrodes in the x-y plane. Each tetrode's placement was determined using a scaffold, ensuring precise targeting of BC (5 tetrodes), the VPM (4 tetrodes), the POm (4 tetrodes), and the ZIv (3 tetrodes). Coordinates were defined with respect to bregma, according to [48] (Table 4). After insertion of the tetrodes into the EIB, tetrodes were fixed using UV-curable adhesive (3M™ Filtek™ Supreme XTE, 3M Deutschland GmbH, Neuss, Germany) and the tungsten wires were then soldered onto the copper traces of the EIB. The tetrodes were then suspended in a gold chloride solution (200 mg/dL gold chloride in deionized water, HT1004-100ML, Sigma-Aldrich, Inc., MO, USA) and

gold plated to reduce their impedances to less than 100kOhm. To ensure proper conductance of the individual channels, a function generator (A365 Stimulus Isolator, World Precision Instruments, Inc., FL, USA) was connected to a basin filled with sodium chloride (120 mM), in which the tetrodes were submerged. Only EIBs with ≥62 conducting channels were used for implantation.

EIB implantation

30 minutes before inducing general anesthesia, buprenorphine hydrochloride (Bupresol vet. Multidose 0,3 mg/ml, 10 ml, CP-Pharma Handelsgesellschaft mbH, Burgdorf, Germany) was administered subcutaneously at a dosage of 0.1 mg/kg of body weight. General anesthesia was induced using isoflurane (1-2 % in oxygen, Isofluran Baxter, Baxter Deutschland GmbH, Germany), with control of the eyelid reflex and pedal withdrawal reflex. Body temperature was monitored and maintained between 36-38 °C. Eye ointment (Bepanthen®, Bayer, Germany) was applied to the eyes and saline solution (30 ml/kg of body weight, Fresenius Kabi Deutschland GmbH, Bad Homburg, Germany) was administered subcutaneously. Lidocaine (Xylocaine® 1%, Aspen Pharma Trading Limited, Ireland) was injected under the scalp to provide local anesthesia in the surgical area. The animal was positioned in a non-traumatic stereotactic alignment apparatus (David Kopf Instruments, Tujunga, CA, USA). Small holes were drilled in the skull over the target areas using a dental drill (78001 Microdrill, RWD Life Science, TX, USA). The tetrodes were then gradually lowered into the brain until the desired depth was reached. The EIB was secured to the skull using a cyanoacrylate-based adhesive (Super-bond, Sun Medical, Japan) and dental cement (Paladur®, Kulzer, Germany). Following the surgeries, animals were placed into their home cage on a heated surface for a minimum of 2 hours before being returned to the ventilated Scantainer. Behavioral experiments started after an adequate period of recovery following the EIB implantation.

Tetrode	A/P	M/L	D/V with respect to dura
BC 1	**- 1.0**	**3.25**	**- 0.4**
BC 2	**- 1.3**	**3.3**	**- 0.3**
BC 3	**- 1.6**	**2.7**	**- 0.85**
BC 4	**- 1.3**	**2.6**	**- 0.85**
BC 5	**- 1.0**	**2.7**	**- 0.85**
VPM 1	**- 1.95**	**1.95**	**- 2.95**
VPM 2	**- 1.95**	**1.6**	**- 2.95**
VPM 3	**- 1.75**	**1.75**	**- 3.0**
VPM 4	**- 1.45**	**1.6**	**- 2.95**
POm 1	**- 2.15**	**1.3**	**- 2.75**
POm 2	**- 2.3**	**1.5**	**- 2.75**
POm 3	**- 2.3**	**1.15**	**- 2.8**
POm 4	**- 2.0**	**1.05**	**- 2.85**
ZIv 1	**- 2.35**	**2.0**	**- 3.7**
ZIv 2	**- 2.6**	**1.75**	**- 3.7**
ZIv 3	**- 2.15**	**1.75**	**- 3.75**

Table 4: Tetrode Coordinates. BC: barrel cortex; VPM: ventral posteromedial nucleus; POm: posterior medial complex; ZIv: ventral zona incerta.

Histology and identification of tetrode positions

After administering a lethal dose of ketamine-xylazine through intraperitoneal injection (ketamine: 120 mg/kg bw, CP-Pharma Handelsgesellschaft mbH, Burgdorf, Germany; xylazine: 20 mg/kg bw, Xylavet® 20 mg/ml, CP-Pharma Handelsgesellschaft mbH, Burgdorf, Germany), a transcardial perfusion with paraformaldehyde (PFA, 4% in phosphate-buffered saline [PBS]) was performed. The mouse's head, along with the EIB implant, was post-fixed

in PFA (4% in PBS) for five days at 4°C. Subsequently, the EIB was removed, the brain was cut into 50 µm thick sections with a vibrating microtome (Thermo Scientific Microm HM 650V), and the tetrode traces were identified using a bright field microscope. Tetrode tracks were manually reconstructed from the microscope images using the Amira software (v6.5, Thermo Fisher Scientific, Waltham, MA). Subsequently, all tetrodes located outside of the designated target areas were excluded from further analysis.

Calcium imaging

Viral Injection

For intracranial viral injections, mice were anesthetized with isoflurane (1 - 2%, Univentor 1200 - anesthesia Unit, Univentor, Zejtun, Malta). Mice were head-fixed in a Kopf Stereotax frame (Model 900, David Kopf Instruments, Tujunga, USA). Deep anesthesia was ensured by the absence of the paw pinch reflex. The head was shaved to expose the skin and disinfected with ethanol swabs. The skin was incised along the rostral-caudal axis of the head, and the surface was cleaned with cotton swabs. An oval-shaped craniotomy was made at (M/L: 1.25, A/P: -1.4 to -2.0, D/V: 3.2) mm relative to bregma using a dental drill (EXL-40, Osada Electric co. ltd.). To achieve optimal expression in POm, we injected the virus solution (AAV-1/2-GCaMP6f, 4.4 x 10^{12} GC, 400 nl) at two coordinates (M/L: 1.25, A/P: -1.4, D/V: 3.2; M/L: 1.25, A/P: -2.0, D/V: 3.2). A pulled glass injection pipette (Puller: Model P-97, Sutter Instrument Co., Novato, USA; Pipette: Blaubrand intraMark micropipettes, product ID 708707) loaded with the virus was slowly lowered to the injection site and the virus was slowly injected (~100 nl/min) by manually applying air pressure with an attached syringe. The tissue was allowed to rest for 10 minutes to facilitate diffusion of the virus before the pipette was slowly pulled back up. The skin was sutured back up with a Braun suture kit.

Grin-Lens Implantation

Two to three weeks after the viral injection, the animal was anesthetized and head-fixed on the Stereotax. A small portion of the skin was removed from the head to expose the skull. The connective tissue was removed with cotton swabs. After adjusting the head in the correct 3D plane, a craniotomy was drilled between the previous injections (M/L: 1.25, A/P: -1.7 relative to bregma). A blunt needle was used to make a leading track for the lens. The needle was advanced with a Luigs & Neumann linear actuator by advancing in 300 µm steps and retracting in 200 µm steps at the speed of 30 µm/s to relieve pressure to a final depth of 3000 µm from the dura. The GRIN lens (Inscopix, product code 1050-004627, ProView™ Lens Probe, 0.5 mm diameter, ~4.0 mm length) was held with a 3D printed custom lens holder. The lens was lowered slowly in the same way as the blunt needle, except for the final depth being 3100 µm. The lens was then fixed to the skull with a self-curing resin cement (Super-bond, Sun Medical, Japan).

Baseplate Implantation

After the GRIN lens implantation, a baseplate was attached to a miniscope, which was lowered while acquiring images through the GRIN lens. The baseplate was lowered to the focal plane and then fixed to the skull with UV-cured dental cement (Gradia Direct Flo, A3, GC Corporation).

Data analysis

The behavioral data was analyzed using custom code developed in MATLAB R2023a (The MathWorks, Inc.), which is available on A-tactile-discrimination-task-to-study-neuronal-

dynamics-in-freely-moving-mice/DataAndScripts at main · GrohLab/A-tactile-discrimination-task-to-study-neuronal-dynamics-in-freely-moving-mice · GitHub [24]. P-values ≤ 0.05 were considered significant. Mean values were reported with standard deviations and median values with interquartile range (IQR).

Statistical analysis of the learning process

Task performance in each session was measured using the discriminability index d-prime (d'), also known as Fisher discrimination index [49,50]. The d' is a statistical measure to quantify the ability to discriminate between signal and noise and is defined as the difference between the z-scores of the hit rate and the FA rate: $d' = z(hit\ rate) - z(false\ alarm\ rate)$. Due to the constraints of the z-score transformation (which cannot handle proportions of 0 or 1), hit rates and FA rates of 0 are typically adjusted to $(\frac{1}{2*n})$ and rates of 1 are adjusted to $(1 - \frac{1}{2*n})$, with n being the number of go- (for hit rate adjustment), or no-go trials (for FA rate adjustment), respectively. A higher d' indicates greater discriminability, meaning the observer can more effectively distinguish signal from noise. A d' of 0 describes a discrimination performance at chance level. An animal was considered to reach expert performance when it crossed a d' of 1.65, corresponding to a one-tailed significance level of α = 0.05.

Success rates for go, no-go trials and all trials were calculated as follows: Hit/(Hit+Miss), CR/(CR+FA) and (Hit+CR)/(Hit+Miss+CR+FA), respectively. The moment of insight was defined as the point where the no-go success rate increases from one session to the other by a factor of 5. To calculate the population moment of insight, each individual moment of insight was interpolated on a common access and then the mean was taken across all mice.

Extraction of behavioral data from videos

Spatial information of the mice was extracted from video recordings using DeepLabCut [23]. Following preprocessing with median background image subtraction, the DeepLabCut model was trained on a subset of manually annotated video frames. For the high-speed videos (240 Hz), these markers consisted of 8 data points for two whiskers on each side from whisker base to tip and markers for the mouse's head contours. To validate tracking accuracy, we estimated the mean average Euclidean error (MAE) between manually annotated labels and DeepLabCut predictions. The estimated MAEs were 3.44 pixels (≈0.3 mm) for the training set and 10.39 pixels (≈1.0 mm) for the test set. We further investigated the consecutive coordinate differences of labels with the inbuilt DeepLabCut function. Instances of label jumps typically affected all labels associated with a specific whisker while preserving their relative spatial arrangement, minimizing the potential impact on our whisker trajectory analysis.

In overview videos, spatial positioning and velocity were estimated based on anatomical landmarks on the mouse's body and head. For the positional data analysis (Fig. 5h), the linear track was divided into rectangles measuring 10 mm by 1 mm. The time spent in each area was calculated by counting the number of video frames in which the mouse was present within each specific rectangle.

Lick events

Trendlines in Fig. 5e were computed with a best-fit asymptotic function: y=a+b·e^(-c·x); where a is the respective median lick latency, b is the initial deviation from the asymptote, and c is the decay rate of latency reduction across trials. The fitting process used least-squares optimization with a MultiStart approach to avoid local minima.

Electrophysiological data

The raw electrophysiological data was spike-sorted with KiloSort 2.0. Subsequently, the sorted clusters were curated automatically using the Ecephys spike sorting algorithm provided by the Allen Brain Observatory (code available at https://github.com/alleninstitute/ecephys_spike_sorting). The algorithm includes noise templates to identify and exclude clusters exhibiting characteristics indicative of noise, such as irregular waveform shapes and interspike interval (ISI) histograms. The following quality metrics were then applied to further exclude any clusters indicative of multi-unit activity: isolation distance (computed from Mahalanobis distance) greater than 15 and ISI violation below 3 %, with an ISI threshold of 1.5 milliseconds. The criteria were selected based on previous studies [51–53], where they have been demonstrated to effectively distinguish well-isolated single units from noise and multi-unit activity. The individual units were further classified into fast spiking (FS) and regular spiking (RS) units, putatively representing inhibitory and excitatory units, respectively[54]. The threshold for differentiating RS from FS units was set to a trough-to-peak duration of 350 µs for cortex and zona incerta, and 300 µs for thalamic nuclei. These thresholds align with previous studies[55,56] and consider the fact that extracellular waveforms in the thalamus are shorter than those in the cortex[55]. For further analysis, only RS units were selected for BC, VPM, and POm, while FS units were selected for ZIv.

Extraction of Calcium Traces and Spatial Footprints

The preprocessing, motion correction, and extraction of the calcium traces and spatial footprints from the videos was done with Minian [57]. All downstream processing was done using custom code developed in MATLAB R2023a (The MathWorks, Inc.).

Detection of Response Onset Latency

To determine the onset latency of neuronal responses following whisker contact, we employed a statistical approach based on a Poisson model of baseline firing rates, similar to de Kock et al., 2007[58]. Firing rates were first binned into bins of 1 ms. The baseline firing rate was then estimated as the mean firing rate within a pre-stimulus window (800 ms to 600 ms before stimulus onset). The first bin within a window of 200 ms after touch onset in which the observed firing rate significantly exceeded the baseline firing rate in a Poisson modelled distribution ($p \leq 0.05$) was identified as the response onset latency.

Touch modulated units

Calcium transients of the POm units were extracted in a window of 400 ms before and after the whisker touch (see above). The summed calcium activity before and after the touch was compared with a paired two-tailed t-test. Whisker touch responsiveness for the extracellular recordings was determined by a statistically significant increase in firing rates (to either of the two aperture states) within a 200 ms response window following aperture touch, compared to a baseline window preceding touch onset. Those units which showed significant differences were identified as touch-modulated units, using a two-sided Wilcoxon signed rank test.

Decoding of aperture width form unit spike trains

Aperture width decoding from unit spike trains traces was conducted using the Neural Decoding Toolbox [59]. The dataset was partitioned into a training set (90% of labels) and a test set (10% of labels). Each set contained the spike traces of individual units for a given trial and the corresponding aperture labels. A support vector machine (SVM) classifier was trained using the LIBSVM software package. The classifier was subjected to a 10-fold cross-

validation, where it was trained and tested on different data partitions. The mean decoding accuracy was then calculated over a window from trigger onset to 400 ms post-trigger onset.

Decoding of aperture width from whisker angles

Aperture width decoding from whisker angles was performed using MATLAB's built-in generalized additive model (GAM) classifier. The dataset was partitioned into a training set (80% of labels) and a test set (20% of labels). Each set included whisker angles recorded 20 frames before and 100 frames after whisker touch, with a sampling rate of 240 fps, along with the corresponding aperture labels. In the shuffled decoding accuracy analysis, the whisker angle traces were randomly allocated to an aperture label. P-values were determined using pointwise 95% confidence intervals, which were computed by the MATLAB "rocmetrics" function based on 100 pointwise bootstrap resamples.

Decoding of aperture width from the calcium imaging data

Calcium transients were extracted 400 milliseconds (12 frames) before and 400 miliseconds (12 frames) after the whisker touch, and a six-layer ReLU-activated convolutional neural network (CNN) was designed and trained for binary classification of calcium transients. The network was provided with the extracted calcium transients from neurons which showed activity during all of the expert sessions. Feature extraction was performed through two convolutional blocks, each consisting of a 3x3 convolutional layer with padding applied to maintain the input dimensions, followed by batch normalization to stabilize learning and a ReLU activation function to introduce non-linearity. Dimensionality was reduced through max pooling layers, which downsampled the feature maps by a factor of 2. Once features were extracted, classification was performed by a fully connected layer with two output neurons, corresponding to the two target classes. A softmax layer was applied to convert the outputs into class probabilities, and predictions were finalized by a classification layer.The network was trained using the stochastic gradient descent with momentum (SGDM) optimizer. Training was conducted over 100 epochs, with an initial learning rate of 0.01.

Analysis of neuronal activity during whisking and quiescence

Whisking behavior was analyzed using a 100 ms moving window, with a 50 ms margin before and after each time point. Periods of free whisking were defined as those with whisking amplitudes exceeding 5° within the specified time window, whereas quiescent periods were characterized by amplitudes below 3°. Frames associated with aperture touch events or occurring within 100 ms of such events were excluded from analysis to minimize potential confounds introduced by touch-related neuronal responses. Statistical significance of whisking angle tuning was determined using a shuffling-based test. Spike times for each unit were shifted by a random interval (uniformly distributed and less than the total recording duration), wrapping the end of the shifted sequence to the beginning of the original sequence. This process preserved spike counts and firing structure while decoupling spikes from behavior. Shuffling was repeated 100 times for each unit. Differences in observed firing rates exceeding the 95th percentile of the shuffled distribution were deemed significant.

Analysis of neuronal activity during locomotion and resting periods

Locomotor activity was quantified using video recordings to extract mouse velocity within a designated region of interest along the linear track. This approach minimized interference from whisker interactions near reward sites or apertures. Velocity estimates were derived using spatial features tracked via DeepLabCut. Locomotion was defined as sustained velocities

exceeding 100 mm/s for longer than 200 ms, while resting was characterized by velocities below 10 mm/s persisting for at least 200 ms. Statistical significance was determined using the same shuffling-based method applied in the analysis of neuronal activity during whisking and quiescence.

Analysis of whisking angle tuning

Whisking angles were analyzed in accordance with prior studies[33]. Angles were binned into 5° intervals, ranging from 0° (maximal retraction) to 180° (maximal protraction). For each bin, firing rates were computed as the number of spikes divided by the total duration within that bin. To exclude touch-related neuronal activity, spikes occurring during or within 100 ms of aperture touch events were excluded. Spikes for each unit were shuffled in the same manner as described above, for statistical testing. Modulation depth $(r_{max} - r_{min})/r_{mean}$, where r_{max} , r_{min} , and r_{mean} are the maximum, minimum, and mean firing rates, respectively, was considered significant if it exceeded the 95th percentile of the shuffled distribution.

Analysis of whisking phase tuning

Whisker position traces were band-pass filtered between 2 and 30 Hz to isolate whisking cycles. Each cycle was divided into 32 bins spanning 360° (or 2π). Instantaneous whisking phase was extracted using the Hilbert transform and normalized to the range [0, 2π]. Spikes were assigned to their corresponding phase bins, and firing rates were calculated for each bin. Phase-dependent modulation of neuronal firing was assessed by fitting a sine wave to the firing rates using linear least-squares regression, as outlined in Moore et al., 2015[60]. In brief the modulation of each unit's activity was quantified by fitting a sine wave with a period of 2π using standard linear least-squares regression. The sine wave fit is defined as:

$$\lambda(t) = \langle\lambda\rangle + Amp_{tuning} \cdot cos(\phi(t) - \phi_{preferred} ,$$

where $\lambda(t)$ represents the mean firing rate, Amp_{tuning} denotes the amplitude of modulation, $\phi(t)$ the whisking phase at time t, and $\phi_{preferred}$ the preferred phase at which the unit's firing is maximally modulated: $\phi_{preferred} = 0$ corresponds to whiskers being fully retracted, and $\phi_{preferred} = \pi$ corresponds to full protraction.

The signal-to-noise ratio (SNR) of the phase tuning was then calculated as:

$SNR = 2 \cdot Amp_{tuning} \sqrt{\frac{T}{\langle\lambda\rangle}}$, where T is the temporal window for a point process with Poisson-distributed spike arrival times, and is estimated from the average whisk cycle to be 111 ms. Statistical significance of modulation was evaluated using a Kuiper test applied to the firing rate distribution across phase bins.

Analysis of head angle tuning

Head angles were categorized into 5° bins, ranging from -90° (head oriented to the left) to 90° (head oriented to the right). For each bin, firing rates were calculated as the number of spikes divided by the total duration spent within the bin. Modulation indices were computed similarly to whisking angle analyses, and significance was assessed using the same shuffling-based procedure. Both allocentric head angle (relative to the environment, measured via high-speed video recordings) and egocentric head angle (relative to the body axis, derived from overview

camera recordings) were analyzed to determine whether neuronal responses differed significantly between these reference frames.

Analysis of spatial tuning

To assess spatial tuning, firing rates were calculated in 100 ms time bins and averaged based on maze position, which was divided into 20 mm spatial bins. Following previous studies the firing rates were modeled using a Gaussian function[61], incorporating an additional linear term to account for speed effects. Units were classified as spatially tuned if the amplitude of the Gaussian fit was significantly different from zero (outside the 95% confidence interval) and the linear speed coefficient was non-significant (within the 95% confidence interval), suggesting a location-specific neuronal response independent of locomotor velocity.

Data availability

All the data are in the manuscript or in supplementary material. Source data is provided as a Source Data file with this paper and under the following links:

https://doi.org/10.5281/zenodo.15051370 [24] and
https://github.com/GrohLab/A-tactile-discrimination-task-to-study-neuronal-dynamics-in-freely-moving-mice/tree/main/DataAndScripts/RawData

Code availability

Code necessary to reproduce the Matlab-generated figures in this study are provided and maintained at:
https://doi.org/10.5281/zenodo.15051370 [24] and
https://github.com/GrohLab/A-tactile-discrimination-task-to-study-neuronal-dynamics-in-freely-moving-mice/tree/main/DataAndScripts

References

1. Temereanca, S. & Simons, D. J. Functional topography of corticothalamic feedback enhances thalamic spatial response tuning in the somatosensory whisker/barrel system. *Neuron* **41**, 639–651 (2004).
2. Larkum, M. E., Zhu, J. J. & Sakmann, B. A new cellular mechanism for coupling inputs arriving at different cortical layers. *Nature* **398**, 338–341 (1999).
3. Bruno, R. M. & Sakmann, B. Cortex is driven by weak but synchronously active thalamocortical synapses. *Science* **312**, 1622–1627 (2006).

4. Mease, R. A., Krieger, P. & Groh, A. Cortical control of adaptation and sensory relay mode in the thalamus. *Proc. Natl. Acad. Sci. U. S. A.* **111**, 6798–6803 (2014).
5. Poulet, J. F. A. & Petersen, C. C. H. Internal brain state regulates membrane potential synchrony in barrel cortex of behaving mice. *Nature* **454**, 881–885 (2008).
6. Banerjee, A. *et al.* Value-guided remapping of sensory cortex by lateral orbitofrontal cortex. *Nature* **585**, 245–250 (2020).
7. Huber, D. *et al.* Sparse optical microstimulation in barrel cortex drives learned behaviour in freely moving mice. *Nature* **451**, 61–64 (2008).
8. de Kock, C. P. J. & Sakmann, B. Spiking in primary somatosensory cortex during natural whisking in awake head-restrained rats is cell-type specific. *Proc. Natl. Acad. Sci. U. S. A.* **106**, 16446–16450 (2009).
9. Oberlaender, M., Ramirez, A. & Bruno, R. M. Sensory Experience Restructures Thalamocortical Axons during Adulthood. *Neuron* **74**, 648–655 (2012).
10. Moore, J. D. *et al.* Hierarchy of orofacial rhythms revealed through whisking and breathing. *Nature* **497**, 205–210 (2013).
11. Borden, P. Y. *et al.* Thalamic bursting and the role of timing and synchrony in thalamocortical signaling in the awake mouse. *Neuron* **110**, 2836–2853.e8 (2022).
12. Ahissar, E., Sosnik, R. & Haidarliu, S. Transformation from temporal to rate coding in a somatosensory thalamocortical pathway. *Nature* **406**, 302–306 (2000).
13. Woolsey, T. A. & Van der Loos, H. The structural organization of layer IV in the somatosensory region (SI) of mouse cerebral cortex. The description of a cortical field composed of discrete cytoarchitectonic units. *Brain Res.* **17**, 205–242 (1970).
14. Xu, N.-L. *et al.* Nonlinear dendritic integration of sensory and motor input during an active sensing task. *Nature* **492**, 247–251 (2012).
15. Petreanu, L. *et al.* Activity in motor-sensory projections reveals distributed coding in somatosensation. *Nature* **489**, 299–303 (2012).
16. Sachidhanandam, S., Sreenivasan, V., Kyriakatos, A., Kremer, Y. & Petersen, C. C. H. Membrane potential correlates of sensory perception in mouse barrel cortex. *Nat.*

Neurosci. **16**, 1671–1677 (2013).

17. Chen, J. L., Carta, S., Soldado-Magraner, J., Schneider, B. L. & Helmchen, F. Behaviour-dependent recruitment of long-range projection neurons in somatosensory cortex. *Nature* **499**, 336–340 (2013).
18. Rodgers, C. C. *et al.* Sensorimotor strategies and neuronal representations for shape discrimination. *Neuron* **109**, 2308–2325.e10 (2021).
19. Hong, Y. K., Lacefield, C. O., Rodgers, C. C. & Bruno, R. M. Sensation, movement and learning in the absence of barrel cortex. *Nature* **561**, 542–546 (2018).
20. Krupa, D. J., Matell, M. S., Brisben, A. J., Oliveira, L. M. & Nicolelis, M. A. Behavioral properties of the trigeminal somatosensory system in rats performing whisker-dependent tactile discriminations. *J. Neurosci.* **21**, 5752–5763 (2001).
21. Krupa, D. J., Wiest, M. C., Shuler, M. G., Laubach, M. & Nicolelis, M. A. L. Layer-specific somatosensory cortical activation during active tactile discrimination. *Science* **304**, 1989–1992 (2004).
22. Klumpp, M. *et al.* Syntalos: a software for precise synchronization of simultaneous multi-modal data acquisition and closed-loop interventions. *Nat. Commun.* **16**, 708 (2025).
23. Mathis, A. *et al.* DeepLabCut: markerless pose estimation of user-defined body parts with deep learning. *Nat. Neurosci.* **21**, 1281–1289 (2018).
24. Heimburg, F. *et al. Supplementary Materials for: 'A Tactile Discrimination Task to Study Neuronal Dynamics in Freely-Moving Mice' (2024)*. (Zenodo, 2024). doi:10.5281/ZENODO.13369686.
25. Rosenberg, M., Zhang, T., Perona, P. & Meister, M. Mice in a labyrinth show rapid learning, sudden insight, and efficient exploration. *Elife* **10**, (2021).
26. Suzuki, M. & Larkum, M. E. General anesthesia decouples cortical pyramidal neurons. *Cell* **180**, 666–676.e13 (2020).
27. Sumser, A., Isaías-Camacho, E. U., Mease, R. A. & Groh, A. Differential representation of active and passive touch in mouse somatosensory thalamus. *bioRxiv* 2024.07.16.603697 (2024) doi:10.1101/2024.07.16.603697.

28. La Terra, D. *et al.* The role of higher-order thalamus during learning and correct performance in goal-directed behavior. *Elife* **11**, (2022).
29. Qi, J., Ye, C., Naskar, S., Inácio, A. R. & Lee, S. Posteromedial thalamic nucleus activity significantly contributes to perceptual discrimination. *PLoS Biol.* **20**, e3001896 (2022).
30. Mo, C., McKinnon, C. & Murray Sherman, S. A transthalamic pathway crucial for perception. *Nat. Commun.* **15**, 6300 (2024).
31. Lou, Y., Caruana, R. & Gehrke, J. Intelligible models for classification and regression. in *Proceedings of the 18th ACM SIGKDD international conference on Knowledge discovery and data mining* 150–158 (ACM, New York, NY, USA, 2012). doi:10.1145/2339530.2339556.
32. Mitchinson, B. *et al.* Active vibrissal sensing in rodents and marsupials. *Philos. Trans. R. Soc. Lond. B Biol. Sci.* **366**, 3037–3048 (2011).
33. Oram, T. B., Tenzer, A., Saraf-Sinik, I., Yizhar, O. & Ahissar, E. Co-coding of head and whisker movements by both VPM and POm thalamic neurons. *Nat. Commun.* **15**, 5883 (2024).
34. Gilad, A., Gallero-Salas, Y., Groos, D. & Helmchen, F. Behavioral strategy determines frontal or posterior location of short-term memory in neocortex. *Neuron* **99**, 814–828.e7 (2018).
35. Isett, B. R., Feasel, S. H., Lane, M. A. & Feldman, D. E. Slip-based coding of local shape and texture in mouse S1. *Neuron* **97**, 418–433.e5 (2018).
36. Park, J. M. *et al.* Deep and superficial layers of the primary somatosensory cortex are critical for whisker-based texture discrimination in mice. *bioRxiv* 2020.08.12.245381 (2020) doi:10.1101/2020.08.12.245381.
37. Oladazimi, M., Brendel, W. & Schwarz, C. Biomechanical Texture Coding in Rat Whiskers. *Sci. Rep.* **8**, 11139 (2018).
38. Ghane-Motlagh, B. & Sawan, M. Design and implementation challenges of microelectrode arrays: A review. *Mater. Sci. Appl.* **04**, 483–495 (2013).
39. Ward, M. P., Rajdev, P., Ellison, C. & Irazoqui, P. P. Toward a comparison of

microelectrodes for acute and chronic recordings. *Brain Res.* **1282**, 183–200 (2009).

40. Geng, J. *et al.* Chronic Ca2+ imaging of cortical neurons with long-term expression of GCaMP-X. *Elife* **11**, (2022).
41. Darainy, M., Manning, T. F. & Ostry, D. J. Disruption of somatosensory cortex impairs motor learning and retention. *J. Neurophysiol.* **130**, 1521–1528 (2023).
42. Morehead, J. R., Qasim, S. E., Crossley, M. J. & Ivry, R. Savings upon re-aiming in visuomotor adaptation. *J. Neurosci.* **35**, 14386–14396 (2015).
43. Jadhav, S. P., Wolfe, J. & Feldman, D. E. Sparse temporal coding of elementary tactile features during active whisker sensation. *Nat. Neurosci.* **12**, 792–800 (2009).
44. Wolfe, J. *et al.* Texture coding in the rat whisker system: slip-stick versus differential resonance. *PLoS Biol.* **6**, e215 (2008).
45. Zuo, Y., Perkon, I. & Diamond, M. E. Whisking and whisker kinematics during a texture classification task. *Philos. Trans. R. Soc. Lond. B Biol. Sci.* **366**, 3058–3069 (2011).
46. Schwarz, C. *et al.* The head-fixed behaving rat--procedures and pitfalls. *Somatosens. Mot. Res.* **27**, 131–148 (2010).
47. Oettl, L.-L. *et al.* Phasic dopamine reinforces distinct striatal stimulus encoding in the olfactory tubercle driving dopaminergic reward prediction. *Nat. Commun.* **11**, 3460 (2020).
48. Paxinos, G. & Franklin, K. B. J. The mouse brain in stereotaxic coordinates. San Diego, Calif. Preprint at (2001).
49. Stanislaw, H. & Todorov, N. Calculation of signal detection theory measures. *Behav. Res. Methods Instrum. Comput.* **31**, 137–149 (1999).
50. Macmillan, N. A. *Detection Theory: A User's Guide*. (Cambridge University Press, Cambridge, England, 1991).
51. Onodera, K. & Kato, H. K. Translaminar recurrence from layer 5 suppresses superficial cortical layers. *Nat. Commun.* **13**, 2585 (2022).
52. Rosenberg, D. M. & Horn, C. C. Neurophysiological analytics for all! Free open-source software tools for documenting, analyzing, visualizing, and sharing using electronic

notebooks. *J. Neurophysiol.* **116**, 252–262 (2016).

53. Trautmann, E. M. *et al.* Accurate estimation of neural population dynamics without spike sorting. *Neuron* **103**, 292–308.e4 (2019).
54. Barthó, P. *et al.* Characterization of neocortical principal cells and interneurons by network interactions and extracellular features. *J. Neurophysiol.* **92**, 600–608 (2004).
55. Barthó, P. *et al.* Ongoing network state controls the length of sleep spindles via inhibitory activity. *Neuron* **82**, 1367–1379 (2014).
56. Mahrach, A., Chen, G., Li, N., van Vreeswijk, C. & Hansel, D. Mechanisms underlying the response of mouse cortical networks to optogenetic manipulation. *Elife* **9**, (2020).
57. Dong, Z. *et al.* Minian, an open-source miniscope analysis pipeline. *Elife* **11**, (2022).
58. de Kock, C. P. J., Bruno, R. M., Spors, H. & Sakmann, B. Layer- and cell-type-specific suprathreshold stimulus representation in rat primary somatosensory cortex: Sensory responses throughout barrel cortex. *J. Physiol.* **581**, 139–154 (2007).
59. Meyers, E. M. The neural decoding toolbox. *Front. Neuroinform.* **7**, 8 (2013).
60. Moore, J. D., Mercer Lindsay, N., Deschênes, M. & Kleinfeld, D. Vibrissa self-motion and touch are reliably encoded along the same somatosensory pathway from brainstem through thalamus. *PLoS Biol.* **13**, e1002253 (2015).
61. Pillow, J. W. & Park, M. Adaptive Bayesian methods for closed-loop neurophysiology. in *Closed Loop Neuroscience* 3–18 (Elsevier, 2016). doi:10.1016/b978-0-12-802452-2.00001-9.

Acknowledgments

We thank Katharina Ziegler for helpful comments on the manuscript. We thank Wolfgang Kelsch and Max Scheller for teaching us the electronic interface board approach as well as Cornelius Schwarz for providing us with the lick ports. This work was supported by the German Research Foundation (DFG Grants GR3757/4-1 to AG and KU 1983/8-1 to TK). We acknowledge the data storage service SDS@hd and high-performance computing initiative bwHPC, supported by the Ministry of Science, Research and the Arts Baden-Württemberg (SDS@hd and bwHPC) and the German Research Foundation (DFG) through grants INST 35/1597-1 FUGG (bwHPC) and INST 35/1503-1 FUGG (SDS@hd). The funders had no role in study design, data collection and analysis, decision to publish, or preparation of the manuscript.

Author information

Authors and Affiliations

Institute for Physiology and Pathophysiology, Heidelberg University, 69120, Germany

Filippo Heimburg, Josephine Timm, Nadin Mari Saluti, Maria Helena Bortolozzo-Gleich, Jesús Martín-Cortecero, Melina Castelanelli, Matthias Klumpp, Lee Embray, Martin Both and Alexander Groh

Institute for Anatomy and Cell Biology, Heidelberg University, 69120, Germany

Avi Adlakha and Thomas Kuner

Institute for Experimental Epileptology and Cognition Research, University of Bonn, 53105, Germany

Current affiliation: Josephine Timm

Contributions

F.H., J.T., N.S., M.C. and A.G. designed the experiments. L.E., F.H., N.S., M.K. and M.C. constructed the setup under supervision of A.G.. M.K. developed Syntalos under supervision of M.B.. J.T., F.H., N.S., M.H.B-G., J.M-C, and A.A. collected and analyzed the data under supervision of A.G.. J.T., F.H., N.S., A.A. and A.G. wrote the paper.

Corresponding author

Correspondence to Alexander Groh

Competing interests

The authors declare that they have no competing interests.

Figure Legends/Captions (for main text figures)

Fig. 1: Tactile discrimination setup and learning paradigm. **a:** Display of the whisker-discrimination setup, created with Blender v2.9 (files can be found here: https://github.com/GrohLab/A-tactile-discrimination-task-to-study-neuronal-dynamics-in-freely-moving-mice [24]). **b:** Rule logic for scoring the choices and triggering the outcomes. **c:** Training scheme with different learning stages and criteria to move to the next stage. **d:** Overview of data acquisition and analysis pipeline for the analysis of task performance, whisker-aperture touch times, head-tracking, single-unit spike times and calcium transients.

Fig. 2: Mice learn to discriminate apertures with their whiskers and learn different task rules. **a:** Mean lick rates from n = 12 mice across three different rule stages. Horizontal dashed lines indicate significant differences. **b:** Success rates over stage progression for Go- (Hit/(Hit+Miss)), No-go (CR/(CR+FA)) and all trials ((Hit+CR)/(Hit+Miss+CR+FA)) (n = 12 mice). Dashed line indicates “moment of insight”, defined by a jump in success rate in no-go trials by a factor of five from one session to the next (n = 5 mice). **c:** Performance over trials for 20 mm contrast. Solid lines show mean d’, calculated with a running window of the preceding 200 trials; shaded areas show standard deviation, horizontal dashed line indicates expert-level performance threshold (d’ = 1.65); n = 12 mice). Animals reached expert-level performance after 471 trials in the initial rule stage and after 1103 trials in the reversed rule stage (dotted vertical lines). **d:** Learning times for initial-, 1st-, 2nd- and 3rd- rule reversal (dotted lines: individual animals; solid lines: means and standard deviation; n = 12 mice). **e:** Performance for initial rule, reversed rule and extinction. Horizontal dashed line indicates expert-level performance threshold (d’ = 1.65). Performance was calculated from the last four sessions in the initial rule and reversed rule stage and the first four sessions in the extinction stage, each dot represents one session, n = 5 mice. **f:** Population performance for mice trained on a gradually decreasing contrast. Horizontal dashed lines indicate chance-level and expert-level performance thresholds (d’ = 0 vs 1.65, respectively). Performance was calculated from the last four sessions in each contrast condition, each dot represents one session, n = 8 mice. **g:** Number of trials required to reach expert-levels for animals trained on different contrasts in the initial and reversed rule.

ns: $p > 0.05$, *: $p \leq 0.05$, **: $p \leq 0.01$ and ***: $p \leq 0.001$; **a:** Welch's t-test, **d, g:** paired t-test, **e:** repeated measures anova, **f:** one-sample t-test. For exact statistics see Supplementary Table 1.

Fig. 3: Neural activity patterns during aperture discrimination task. **a:** Schematic representation of a head-mounted EIB. **b:** Representative raster plots of single unit spiking activity in BC, VPM, POm, and ZIv, aligned to the time of whisker-aperture contact (magenta line). Below each raster plot, corresponding PSTHs display mean firing rates. **c:** Onset latencies of neuronal responses following whisker contact with the aperture across different brain regions. Latencies were computed based on the first significant deviation from baseline activity (see Methods). Violin plots depict the distribution of response latencies, with mean values highlighted as bars, and median with IQR as filled circles with whiskers. **d:** Schematic representation of a head-mounted UCLA Miniscope V4. **e:** Spatial footprints of POm units from one example imaging session (left), with four touch-modulated units highlighted in color. Example normalized calcium transients (ΔF/F0) from the four touch-modulated POm units (middle), with magenta lines indicating whisker touches with the aperture. Trial-aligned calcium transients of a representative POm unit and averaged across trials below. Lick onsets are marked in blue. **f:** Population PSTHs displaying the mean firing rate (± SEM) of different brain areas, for wide (green) and narrow aperture trials (red), over all expert sessions. Neural activity is aligned to the time of whisker-aperture contact. For POm, normalized calcium activity (±SEM) from 39 POm neurons detected in a single session is shown. **g:** Venn diagrams showing proportions of touch-modulated units/neurons per brain region (from a total sample indicated by black circles). Units/neurons responding selectively to the wide aperture are shown in green, those responding to the narrow aperture in red. The intersection represents units responsive to both apertures.

Fig. 4: Intact whisker input and barrel cortex are necessary for normal task performance and learning. **a:** Population performance for expert animals before and after bilateral whisker-pluck. Performance calculated from last session before and first session after the whisker pluck, each dot represents one session, dashed line indicates expert-level threshold (d' = 1.65), n = 6 mice. **b:** Same as in a but with unilateral whisker pluck and for contrasts of 6 and 20 mm (n = 4 mice for each contrast). **c:** Same as in a but with barrel cortex ablations (red) or sham operations (grey). **d:** Performance over trials in barrel cortex ablated mice (red) and sham operated animals (grey). Expert-level performance (d' = 1.65, grey horizontal dashed line) was crossed after 478 vs. 2023 trials for sham (grey vertical dashed line) and ablated mice (red vertical dashed line), each n= 4 mice. Inset: example reconstruction of barrel cortex ablation. **e:** Population performance for expert animals in d, calculated from the session with the maximum d prime for each mouse (n = 4 mice each). **f:** Population performance for expert animals (n = 4 mice) with alternating application of lidocaine or neutral ointment (control) to the whisker pad. Performance was calculated from 7 lidocaine and 7 control sessions across all mice for each condition. Same conventions as in a. **g:** Time-resolved decoding accuracy of aperture width from spike data of different brain areas. Spike data was analyzed from expert sessions (800 ms before to 400 ms after aperture touch). **h:** Receiver operating characteristic curves from a generalized additive model classifier based on whisker angles after whisker-touch onset. Comparison of control (black), lidocaine sessions (orange), and randomly shuffled labels (light gray). Accuracies for control and lidocaine sessions were not significantly different from each other, but both differed significantly from the shuffled accuracies (n = 3 mice). **i**: Decoding accuracy from spike data for lidocaine sessions (orange boxes) and control sessions (black boxes). The mean decoding accuracy was calculated over a time window from trigger onset to 400 ms post-trigger onset (see Methods). Number of units (from n = 3 mice) in lidocaine sessions: 128 (BC), 100 (VPM), 52 (POm), 17 (ZIv); and control sessions: 150 (BC), 101 (VPM), 64 (POm), 17 (ZIv).

ns: $p > 0.05$, *: $p \leq 0.05$, **: $p \leq 0.01$ and ***: $p \leq 0.001$; **a, b:** two-tailed paired t-test, **c:** two-way anova, **e:** independent samples t-test, **f:** repeated measures anova, **i:** two-tailed Wilcoxon rank sum test. For exact statistics see Supplementary Table 1.

Fig. 5: Capturing naturalistic decision-making, active touch strategies, and dynamic behavioral states during learning. **a:** Approaching behavior to the lick spout following whisker contact ("Touch") with the aperture in a CR trial, shown for a naive session (left) and an expert session (right). The blue trace represents the snout trajectory over time. Retraction time and distance are quantified from the maximum of the trajectory (= turning point), with respect to the beam break (retraction time) and aperture position (retraction distance). **b:** Retraction times across different learning stages (chance, good, expert). **c:** Same as b for Retraction distances (mean with 95%CI). **d:** Example lick latencies from one mouse after whisker-aperture interaction (t = 0 ms) for an early (naive, left) and an expert session (right). Go trials are highlighted in green, no-go trials in red. **e:** Population lick latencies (n = 6 mice) following whisker-aperture interaction (t = 0ms) across the initial learning stage for Hit (green) and FA (red) trials. Trials are grouped into four equal bins based on trial progression for statistical comparison between early (bottom) and late (top) trials. Trendlines (green and red) represent the best-fit asymptotic function (see methods). **f:** Example whisker angle and aperture touches (magenta) during a hit trial (averaged angle values α from four DeepLabCut-tracked whiskers). **g:** Number of whisking cycles during CR and FA trials (mean with 95%CI) in naive (initial 4 sessions) and expert sessions (final 4 sessions). **h:** Heat map of positional data along the linear track of the setup of an exemplary session. The color indicates the time spent in that area (see Methods). The corresponding mean velocity across the track is shown below. **i:** Representative examples of spatially tuned units, showing firing rates as a function of position relative to the middle point (mm), with firing rate histograms and fitted gaussian tuning curves (black). **j:** Proportion of spatially tuned units across all recorded brain regions. Each dot represents the mean proportion for an individual animal, with the cohort mean ± standard deviation as colored bars. **k:** Firing rates during rest (R) and locomotion (L), across brain regions. Each dot represents the firing rate of a single unit (non-significant units in grey, significant units in color). Pie charts indicate the proportion of significantly modulated units (E: enhanced activity; S: suppressed activity). Solid lines connect mean firing rates during R and L for significantly modulated units.

ns: $p > 0.05$, *: $p \leq 0.05$, **: $p \leq 0.01$ and ***: $p \leq 0.001$; **b, c, g:** two-tailed Wilcoxon rank sum test, **e:** Kruskal-Wallis Test, **k:** two-tailed paired t-test; n = 413 (BC), 420 (VPM), 261 (POm), and 147 (ZIv) units in total. Data was pooled from n = 6 mice. For exact statistics see Supplementary Table 1.

Fig. 6: Neural encoding of whisker- and head kinematics during active sensory exploration. **a:** Representative examples of whisker angle tuning in the VPM, showing firing rates of a tuned unit (top) and non-tuned unit (bottom) as a function of whisker angle with null distributions (grey, mean ± SEM). **b:** Proportion of units significantly tuned to whisker angle in the BC, VPM, POm, and ZIv (see Methods). Each dot represents the mean proportion for an individual animal, with the cohort mean ± standard deviation as colored bars. **c:** Examples of whisker phase tuning in the BC, with firing rates plotted for a tuned unit (left) and a non-tuned unit (right) across whisker phases. A sinusoidal function is fitted to the respective distribution. **d:** Proportion of units significantly tuned to whisker phase in the BC, VPM, POm, and ZIv. Representations follow the logic of Fig. 6b. **e:** Polar plots of phase-tuned units across brain regions, displaying individual vectors (grey arrows) and the mean population vector (colored arrows) of whisker phase tuning. **f:** Proportion of units tuned to head azimuth with egocentric (left) and allocentric (right) references across BC, VPM, POm, and ZIv. Representations follow the logic of Fig. 6b.

a: Test against null-distribution of shuffled spike times (see Methods), **c:** Kuiper test; n = 413 (BC), 420 (VPM), 261 (POm), and 147 (ZIv) units in total. Data pooled from n = 6 mice.

Supplementary Materials

A tactile discrimination task to study neuronal dynamics in freely-moving mice

Filippo Heimburg*[,1], Nadin Mari Saluti*[,1], Josephine Timm*[,1,2], Avi Adlakha [3], Maria Helena Bortolozzo-Gleich[1], Jesús Martín-Cortecero[1], Melina Castelanelli[1], Matthias Klumpp[1], Lee Embray[1], Martin Both[1], Thomas Kuner[3] and Alexander Groh[1]

*first authors

[1] Institute for Physiology and Pathophysiology, Heidelberg University, 69120, Germany

[2] Current address: Institute for Experimental Epileptology and Cognition Research, University of Bonn, 53105, Germany

[3] Institute for Anatomy and Cell Biology, Heidelberg University, 69120, Germany

groh@uni-heidelberg.de (AG)

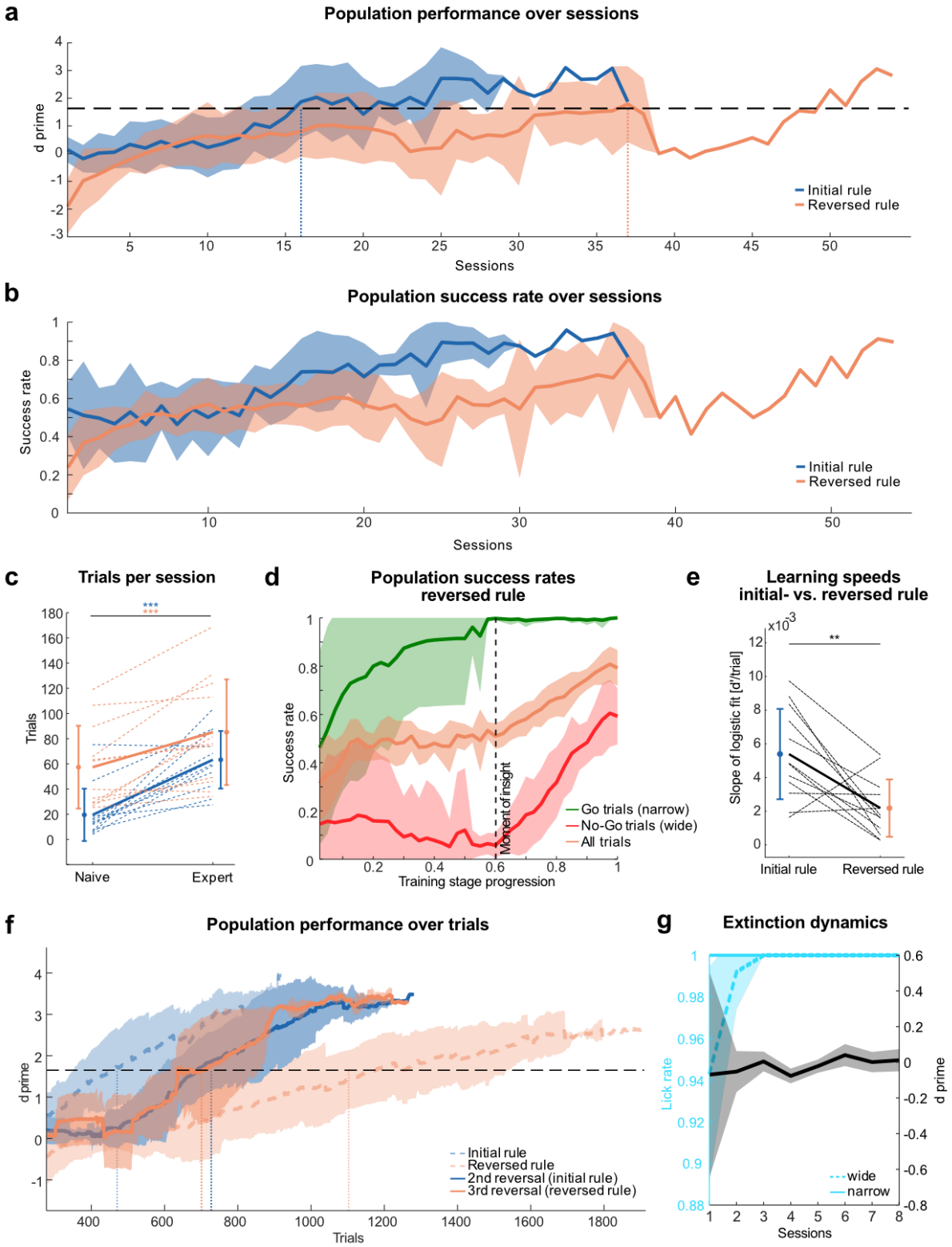
a
Population performance over sessions
d prime
Sessions
Initial rule
Reversed rule
b
Population success rate over sessions
Success rate
Sessions
Initial rule
Reversed rule
c
Trials per session
Trials
Naive
Expert
d
Population success rates reversed rule
Success rate
Training stage progression
Moment of insight
Go trials (narrow)
No-Go trials (wide)
All trials
e
Learning speeds initial- vs. reversed rule
Slope of logistic fit [d'/trial]
Initial rule
Reversed rule
f
Population performance over trials
d prime
Trials
Initial rule
Reversed rule
2nd reversal (initial rule)
3rd reversal (reversed rule)
g
Extinction dynamics
Lick rate
d prime
Sessions
wide
narrow

Supplementary Fig. 1: Learning curves for initial and repeated rule reversals. **a:** Population performance over sessions for a contrast of 20 mm. Solid lines show mean d'; shaded areas show standard deviation (horizontal dashed line: expert-level performance threshold (d' = 1.65); n = 12 mice). Animals reached expert-level performance after 16 sessions in the initial rule stage and after 37 sessions in the reversed rule stage (dotted vertical lines). **b:** Population success rates over sessions for a contrast of 20 mm. Solid lines show mean d'; shaded areas show standard deviation (n = 12 mice). **c:** Trials per session during the initial and reversed rule stage for naive and expert animals (dotted lines: paired values of individual animals; solid line: paired values of population means; data points with error bars: population means and standard deviations; n = 12 mice). **d:** Success rates over stage progression for Go- (Hit/(Hit+Miss)), No-go (CR/(CR+FA)) and all trials ((Hit+CR)/(Hit+Miss+CR+FA)) (n = 12 mice). Dashed line indicates "moment of insight", defined by a jump in success rate in no-go trials by a factor of five from one session to the next (n = 7 mice).**e:** Learning speeds for initial and reversed rules (same conventions as in b; n = 12 mice). **f:** Population performance over trials for initial-, 1st- 2nd- and 3rd-rule reversal. Mean d' calculated with a running window of the preceding 200 trials; shaded areas show standard deviation (horizontal dashed line: expert-level performance threshold (d' = 1.65); n = 12 mice for initial and reversed, 5 mice for 2nd reversal, 2 mice for 3rd reversal). Animals reached expert-level performance after 388 trials in the initial rule stage, after 1077 trials in the reversed rule stage, after 728 trials in the 2nd reversal and after 701 trials in the 3rd reversal (dotted vertical lines). **g:** Mean lick rates (wide (previous No-go), narrow (previous Go)) and d prime over extinction sessions (n = 5 mice).

ns: $p > 0.05$, *: $p \leq 0.05$, **: $p \leq 0.01$ and ***: $p \leq 0.001$; **a:** two-tailed Wilcoxon rank sum test, **d, e:** paired t-test. For exact statistics see Supplementary Table 1.

.

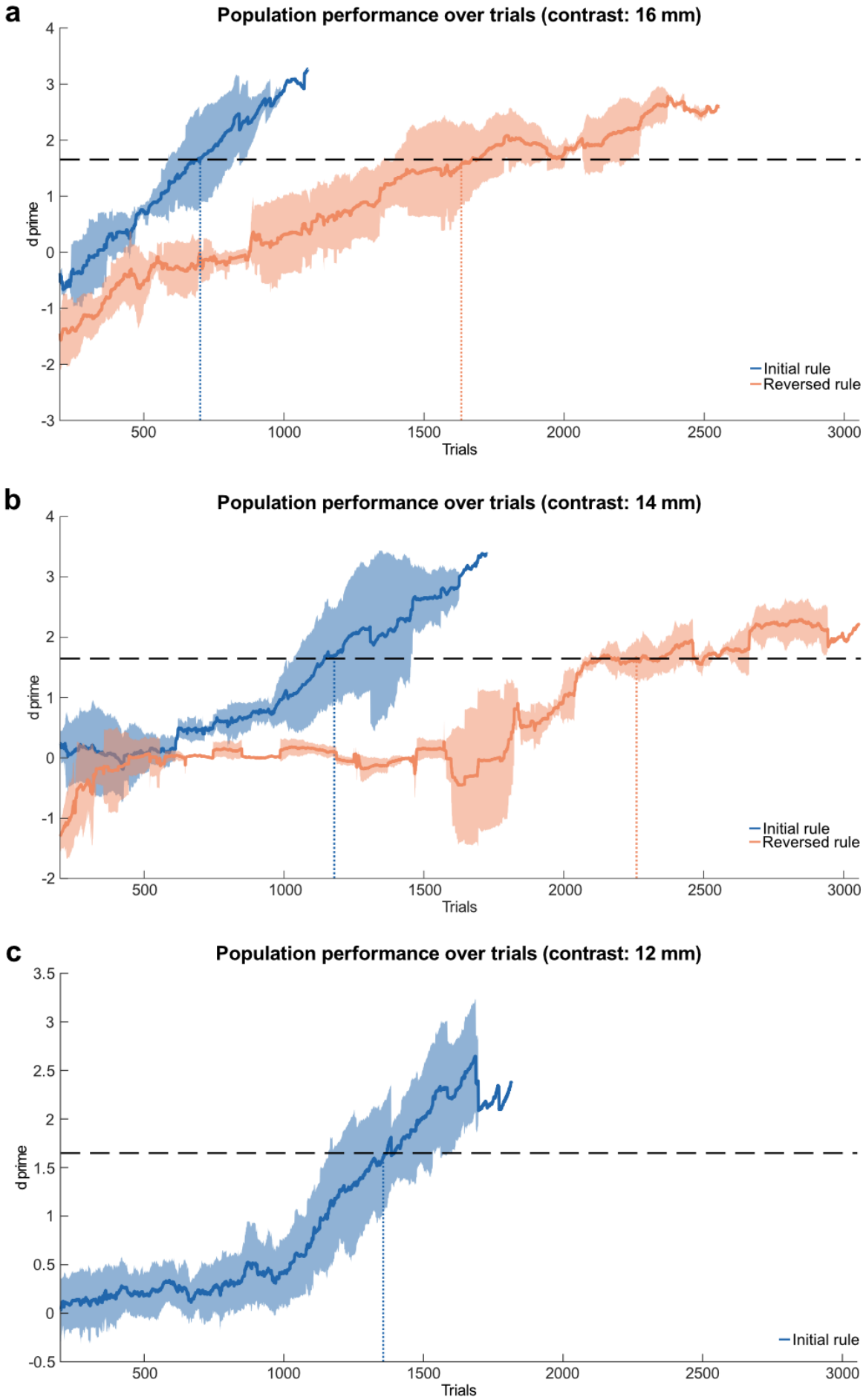
a
Population performance over trials (contrast: 16 mm)
d prime
Trials
Initial rule
Reversed rule
b
Population performance over trials (contrast: 14 mm)
d prime
Trials
Initial rule
Reversed rule
c
Population performance over trials (contrast: 12 mm)
d prime
Trials
Initial rule

1332

Supplementary Fig. 2: Learning curves for different contrasts. **a:** Population performance over trials for 16 mm contrast. Solid lines show mean d', calculated with a running window of the preceding 200 trials; shaded areas show standard deviation (initial rule: blue and reversed rule: orange; horizontal line: expert-level performance threshold (d' = 1.65); n = 3 mice). Animals reached expert-level performance after 701 trials in the initial rule stage and after 1633 trials in the reversed rule stage (dotted vertical lines). **b:** Same as in A for 14 mm contrast (n = 3 mice (initial rule) and 2 mice (reversed rule)). Animals reached expert-level performance after 1180 trials in the initial rule stage and after 2260 trials in the reversed rule stage (dotted vertical lines). **c:** Same as in A, B for 12 mm contrast (n = 6 mice). Animals reached expert-level performance after 1356 trials in the initial rule stage (dotted vertical line).

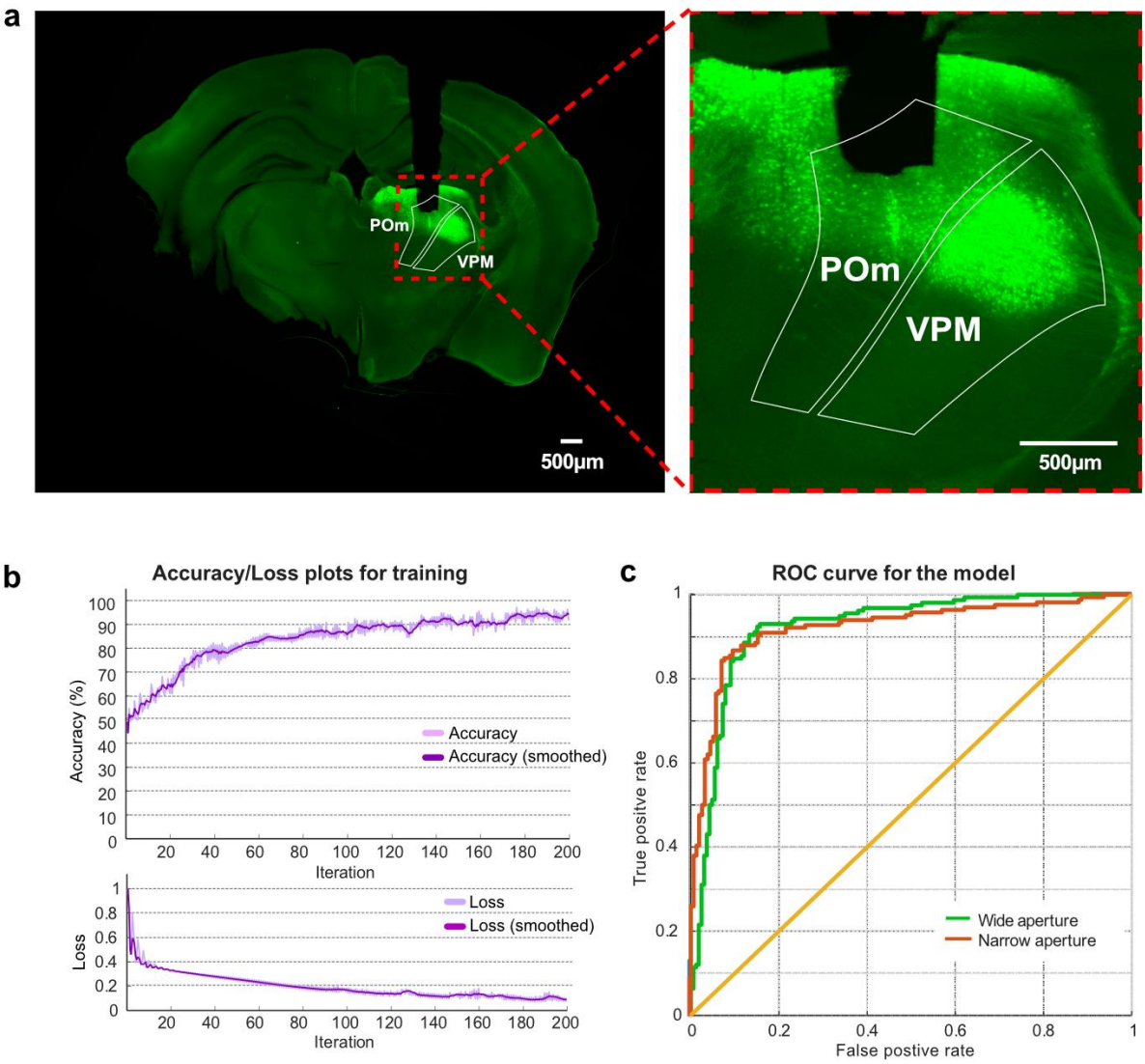

Supplementary Fig. 3: Miniscope imaging during aperture discrimination learning task. **a:** Left: Coronal section of example mouse brain slice, indicating the tract of the GRIN lens, and the recording region for GCamp6f (green) calcium imaging in POm. Right: same as left at higher magnification. **b:** The convolutional neural network (CNN) classifier for aperture width using calcium imaging data. Shown are Accuracy/Loss plots for the training of the CNN classifier. **c:** The ROC statistic curve for classification of the two apertures.

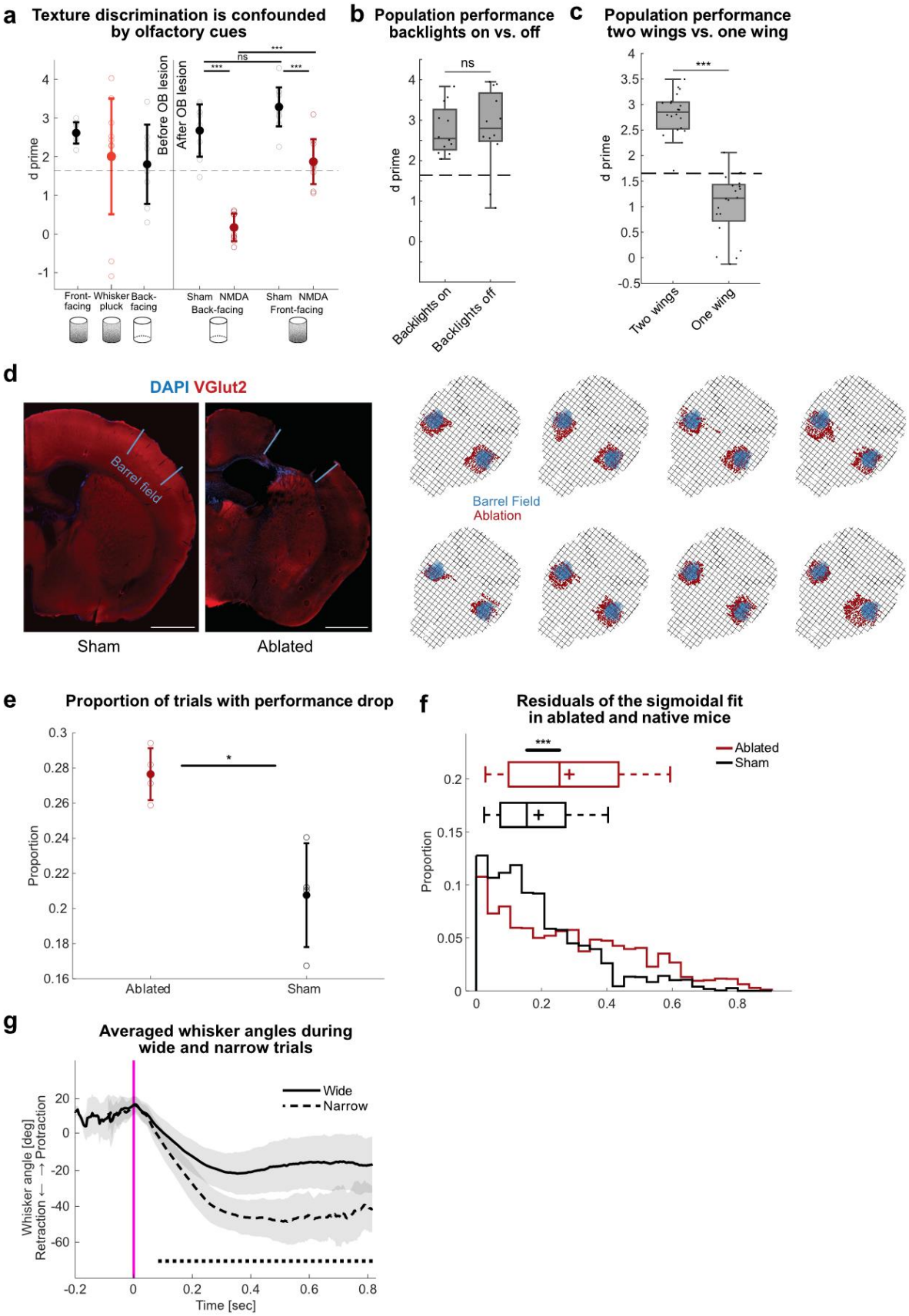
a
Texture discrimination is confounded by olfactory cues
d prime
Before OB lesion
After OB lesion
Front-facing
Whisker pluck
Back-facing
Sham
NMDA
Back-facing
Sham
NMDA
Front-facing
ns
***
b
Population performance backlights on vs. off
ns
Backlights on
Backlights off
c
Population performance two wings vs. one wing
***
Two wings
One wing
d
DAPI VGlut2
Barrel field
Sham
Ablated
Barrel Field
Ablation
e
Proportion of trials with performance drop
Proportion
*
Ablated
Sham
f
Residuals of the sigmoidal fit in ablated and native mice
***
Ablated
Sham
Proportion
g
Averaged whisker angles during wide and narrow trials
Wide
Narrow
Whisker angle [deg]
Retraction ← → Protraction
Time [sec]

1350

Supplementary Fig. 4: Increased performance variability in ablated mice. **a:** Performance before and after olfactory bulb (OB) lesion with NMDA (red) or sham injections with saline (black) during sandpaper texture discrimination (n = 2 mice). Before OB lesion, mice discriminated both the-front facing and inverted (back-facing) textures with similar accuracy. Following OB lesions, performance was completely abolished, while sham-lesioned mice retained discrimination ability. Performance was restored when sandpapers were presented in their original orientation (front-facing. Each dot represents an individual session, with mean ± standard deviation shown. **b:** Performance of expert animals with backlights on and off. Horizontal dashed line indicates expert-level performance threshold (d' = 1.65). Performance was calculated from the last two sessions with backlights on and the first two sessions with backlights off, each dot represents one session. **c:** Performance of expert mice (n = 5 mice) with two aperture wings or one aperture wing. Performance was calculated from in total 20 sessions across all mice for each condition. **d:** Barrel cortex ablations: Coronal sections (60µm) of eight ablated brains were imaged, and the barrel field was visualized using an anti-vGlut2 stain (left panel: example of a sham and ablated section). The extent of the barrel field (blue) and the ablation (red) were annotated in each section. Sections and annotations were then registered and visualized using the Allen CCF framework (https://github.com/cortex-lab/allenCCF) for all eight ablated brains (right panel). **e:** Proportion of trials that were followed by a performance drop in ablated (red) and control (black) mice. Ablated mice exhibited a significantly greater proportion of trials associated with performance drops compared to controls. Each dot represents an individual mouse, with error bars indicating mean ± 95% CI (0.28±0.01 for ablated mice; 0.21±0.03 for control mice). **f:** Distribution of residuals from the sigmoidal fit to trial performance in ablated (red) and control (black) mice. Ablated mice exhibited significantly larger residuals, indicative of heightened performance variability. Box plots display the median (central line) and mean (cross). **g:** Average whisker angles upon encountering the wide (solid) or narrow (dashed) aperture, with mean ± standard deviation. Horizontal dashed lines indicate significant differences.

ns: $p > 0.05$, *: $p \leq 0.05$, **: $p \leq 0.01$ and ***: $p \leq 0.001$; **a:** two-tailed Wilcoxon rank sum test, **b:** paired t-test, **c:** repeated measures anova, **d, f:** two-tailed Wilcoxon rank sum test, **g:** Welch's t-test; if not stated otherwise, data was pooled from n = 6 mice. For exact statistics see Supplementary Table 1.

Supplementary Fig. 5: Firing rates during quiescence and whisking. Firing rates during quiescence and whisking across four brain regions. Each dot represents the firing rate of a single unit (non-significant units in grey, significant units in color). Pie charts above display the proportion of significantly modulated units (E: significantly enhanced activity; S: significantly suppressed activity). Solid lines connect the mean values for quiescence (left) and whisking (right) of significantly modulated units. Significant increases in mean population firing rates during whisking are marked by asterisks.

*: $p \leq 0.05$, ***: $p \leq 0.001$; two-tailed paired t-test; n = 413 (BC), 420 (VPM), 261 (POm), and 147 (ZIv) units in total, pooled from n = 6 mice. For exact statistics see Supplementary Table 1.

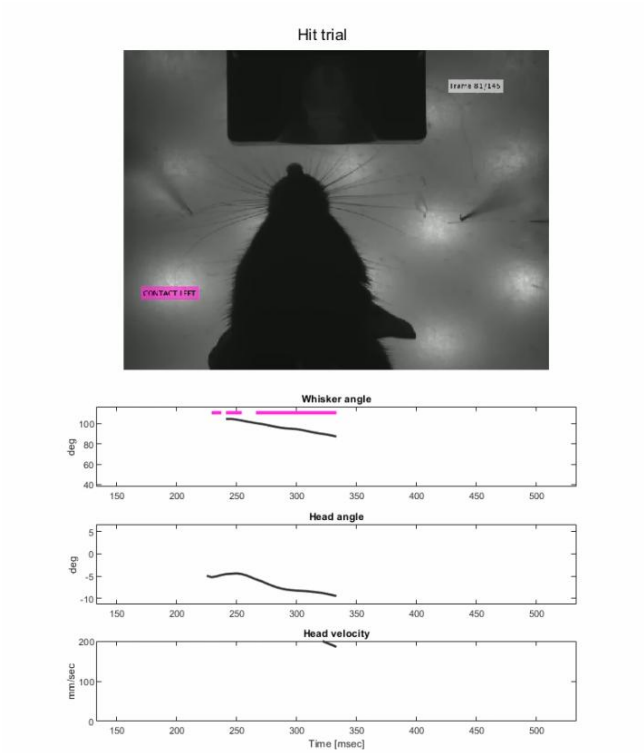

Supplementary video 1: High-speed camera video depicting a hit trial, recorded at 240 FPS and slowed down by a factor of 10 for video playback. The mouse identifies the rewarded aperture and licks lick port to obtain the reward. The accompanying plots display: (1) the average whisker angle relative to the whisker pad (protraction indicated by greater whisker angles), (2) the head angle relative to the midline (values >0° indicate a rightward tilt), and (3) the velocity of the mouse's head within the field of view.

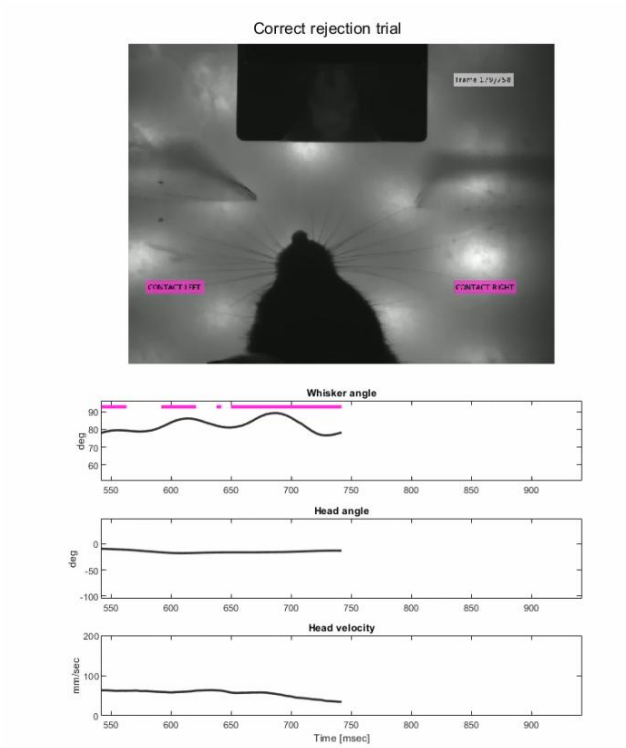

Supplementary video 2: High-speed camera video depicting a correct rejection (CR) trial, recorded at 240 FPS and slowed down by a factor of 10 for video playback. The mouse identifies the punished aperture and turns away from the lick port. The accompanying plots display: (1) the average whisker angle relative to the whisker pad (protraction indicated by greater whisker angles), (2) the head angle relative to the midline (values >0° indicate a rightward tilt), and (3) the velocity of the mouse's head within the field of view.

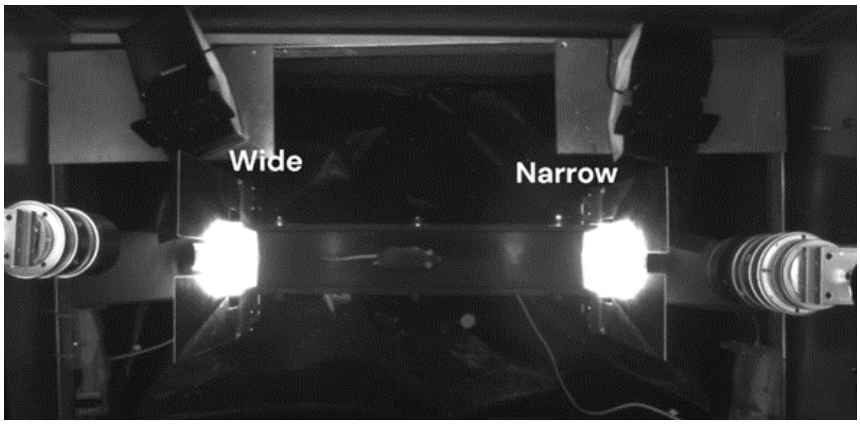

Supplementary video 3: Overview camera video illustrating the experimental setup, recorded at 60 FPS and accelerated by a factor of 2 during video playback. The mouse alternately navigates a linear track to obtain rewards and avoid punishments based on the aperture state. The aperture state, determined by the width of the wing's cleft, changes automatically and randomly between two states. Speakers for administering punishment were positioned behind the linear track. High-speed cameras were positioned overhead at the reward retrieval sites to track whisker-aperture interactions during stimulus sampling.

Figure	Groups	Test statistic, p values, 95% confidence interval (95%CI)	Statistical test
2a	go trials vs. no-go trials	initial rule: $p < 0.05$ for 70%-100% training stage progression reversed rule: $p < 0.05$ for 60%-100% training stage progression	Welch's t-test
2a	go trials vs. neutral trials	$p < 0.05$ for complete stage	Welch's t-test
2a	no-go trials vs. neutral trials	$p < 0.05$ for complete stage	Welch's t-test
2d	initial vs. reversed rule intercept	t-statistic = -7.1879, $p = 1{,}77 \times 10^{-5}$, 95%CI of the true mean difference = [-825.9572; -438.7095]	two-tailed, paired t-test
2d	initial rule vs. second reversal intercept	t-statistic = -5.5581, p = 0.0051, 95%CI of the true mean difference = [-517.9390; -172.8610]	two-tailed, paired t-test
2d	initial rule vs. third reversal intercept	t-statistic = -6.2991, p = 0.1002, 95%CI of the true mean difference = [-1.1118×10^{3}; 374.8130]	two-tailed, paired t-test

2d	reversed rule vs. second reversal intercept	t-statistic = 3.3183, p = 0.0294, 95%CI of the true mean difference = [56.5671; 636.2329]	two-tailed, paired t-test
2d	reversed rule vs. third reversal intercept	t-statistic = 0.6548, p = 0.6309, 95%CI of the true mean difference = [-4.3988×10^3; 4.8768×10^3]	two-tailed, paired t-test
2d	second vs. third reversal intercept	t-statistic = -0.3057, p = 0.8111, 95%CI of the true mean difference = [-2.5113×10^3; 2.3933×10^3]	two-tailed, paired t-test
2e	Initial vs. extinction sessions	F-statistic = 2171.411, p = 0.000, 95%CI of the true mean difference = [2.241; 2.923]	repeated measures anova
2e	Reversed vs. extinction sessions	F-statistic = 2171.411, p = 0.000, 95%CI of the true mean difference = [1.869; 2.732]	repeated measures anova
2f	Comparison against 0	20 mm: p = 7.2618×10^{-24} 16 mm: p = 1.4955×10^{-22} 12 mm: p = 7.9206×10^{-26} 10 mm: p = 2.1662×10^{-24} 8 mm: p = 1.3793×10^{-24} 6 mm: p = 8.4266×10^{-22} 4 mm: p = 8.3217×10^{-12} 2 mm: p = 0.0681	one-sample t-test
2g	Initial vs. reversed rule intercept (contrats = 20)	t-statistic = -7.1879, p = $1{,}77 \times 10^{-5}$, 95%CI of the true mean difference = [-825.9572; -438.7095]	two-tailed, paired t-test
2g	Initial vs.reversed rule intercept (contrats = 16)	t-statistic = -5.7857, p = 0.0286, 95%CI of the true mean difference = [-1625.68; -238.9859]	two-tailed, paired t-test
3c	Onset latencies upon aperture touch [ms]	Median [IQR] BC: 27.5 [8.5;56.5] VPM: 18.5 [6.5; 43.5] POm: 20.5 [5.5; 46.5] ZIv: 15.5 [5.5; 60.75] Mean BC: 40.8308 VPM: 35.2179 POm: 35.3440 ZIv: 37.6185	
4a	Pre pluck vs. post pluck	t-statistic = 13.6362, p = 3.8×10^{-5}, 95%CI of the true mean difference = [1.9665; 2.8802]	two-tailed, paired t-test
4b	Pre pluck vs post uni-lateral pluck	6 mm: t-statistic = 12.3257, p = 0.0012, 95%CI of the true mean difference = [1.3847; 2.3486] 20 mm: t-statistic = 2.9846, p = 0.058, 95%CI of the true mean difference = [-0.0885; 2.7582]	two-tailed, paired t-test

4c	Before vs. after sham/ablation	Group (sham/ablation): F-statistic = 4.4580, p = 0.0564, η^2 = 0.1054 Condition (before/after): F-statistic = 19.6032, p = 8.2×10^{-4}, η^2 = 0.4637 Sham before vs. Ablation after: mean difference = 1.7980, p = 0.0028, 95%CI = [0.6436, 2.9525] Sham after vs. Ablation after: mean difference = 1.9030, p = 0.0018, 95%CI = [0.7485, 3.0575] Ablation before vs. ablation after: mean difference = 1.2662, p = 0.0303, 95%CI = [0.1117, 2.4207]	two-way anova Tukey's HSD test for multiple comparisons
4e	Maximum d prime sham vs. ablation	t-statistic = 3.1176, p = 0.0206, 95%CI of the true mean difference = [0.1933; 1.6038]	independent samples t-test
4f	Bepanthen vs. lidocaine sessions	t-statistic = 3.9892, p = 0.0282, 95%CI of the true mean difference = [0.3585; 3.1870]	two-tailed paired t-test with means for each animal
4h	Lidocaine sessions Control sessions Shuffled labels	Mean AUC = 0.8687, 95%CI = [0.8207, 0.9050] Mean AUC = 0.9059, 95%CI = [0.8590, 0.9304] Mean AUC = 0.5303, 95%CI = [0.4580, 0.6216]	
4h	Lidocaine vs. control	t-statistic = -1.6676, p = 0.0972	two-tailed, two-sample t-test
4h	Control vs. shuffled	t-statistic = 7.7886, p = 3.5392×10^{-12}	two-tailed, two-sample t-test
4h	Lidocaine vs. shuffled	t-statistic = 6.7526, p = 4.4247×10^{-10}	two-tailed, two-sample t-test
4i	BC	t-statistic = 9.2115, p = 9.2337×10^{-5}, 95%CI of the true mean difference = [15.9986; 27.5728]	two-tailed, paired t-test
4i	VPM	t-statistic = 8.4932, p = 1.4578×10^{-4}, 95%CI of the true mean difference = [10.2717; 18.5855]	two-tailed, paired t-test
4i	POm	t-statistic = 3.2869, p = 0.0167, 95%CI of the true mean difference = [2.7197; 18.5660]	two-tailed, paired t-test
4i	ZIv	t-statistic = 4.1617, p = 0.0059, 95%CI of the true mean difference = [4.4735; 17.2408]	two-tailed, paired t-test
5b	Comparison of retraction times [s]	Median [Q1; Q3] = 6.91 [3.64; 27.03] (chance) 1.78 [0.83; 2.95] (good) 1.27 [0.56; 2.43] (expert) p = 0.0268 (expert vs. good) 2.5879×10^{-6} (expert vs. chance)	two-tailed Wilcoxon rank sum test

5c	Comparison of retraction distances [mm]	Mean ± 95%CI = 2.75±7.51 (chance) -0.31±1.49 (good) -2.00±0.41 (expert) p = 0.2251 (expert vs. good) 0.0277 (expert vs. chance)	two-tailed Wilcoxon rank sum test
5e	Lick latencies in the different trial quarters of the initial learning stage	Chi-square = 327.82, p = 9.4617×10^{-71} Quarter 1 vs. quarter 2, p = 1.3660×10^{-8} Quarter 1 vs. quarter 3, p = 0.0000 Quarter 1 vs. quarter 4, p = 0.0000	Friedman test Dunn-Sidak-adjusted multiple comparisons
5g	Naive CR vs. naive FA	p = 2.3356×10^{-8}	two-tailed Wilcoxon rank sum test
5g	Expert CR vs. expert FA	p = 0.5762	two-tailed Wilcoxon rank sum test
5g	Naive CR vs. expert CR	p = 1.7981×10^{-6}	two-tailed Wilcoxon rank sum test
5g	Naive FA vs. expert FA	p = 0.2900	two-tailed Wilcoxon rank sum test
5k	Firing rates during rest and locomotion	Significantly enhanced cells: 21/413 (BC), 66/420 (VPM), 42/261 (POm), 17/147 (ZIv) Significantly suppressed cells: 30/413 (BC), 24/420 (VPM), 10/261 (POm), 4/147 (ZIv) Mean rest firing rate [Hz]: 17.21 (BC), 18.71 (VPM), 12.81 (POm), 6.64 (ZIv) Mean locomotion firing rate [Hz]: 14.93 (BC), 30.67 (VPM), 26.98 (POm), 20.57 (ZIv) p = 0.33 (BC), 4.1478×10^{-5} (VPM), 4.4448×10^{-7} (POm), 0.0036 (ZIv)	two-tailed paired t-test
6f	Proportions of tuned units (egocentric)	11.2±8.7% in BC, 6.8±4.2% in VPM, 5.4±5.5% in POm, 7.2±5.6% in ZIv	
6f	Proportions of tuned units (allocentric)	12.0±8.8% in BC, 6.2±4.6% in VPM, 6.2±5.2% in POm, 1.7±2.4% in ZIv	
S1c	Naive vs. expert trials per sessions	initial rule: t-statistic = -5.4562, p = 1.99×10^{-4}, 95%CI of the true mean difference = [-61.369; -26.0893] reversed rule: t-statistic = -1.6198, p = 0.1336, 95%CI of the true mean difference = [-10.8114; 1.6447]	two-tailed, paired t-test
S1e	Initial vs. reversed rule learning speed	t-statistic = 3.4331, p = 0.0056, 95%CI of the true mean difference = [0.0012; 0.0053]	two-tailed, paired t-test

S4a	Performance upon OB lesion	Mean ± Std Normal textures: 2.61±0.28 Inverted textures: 1.80±1.03 Inverted textures (post-injection) Sham: 2.68±0.68 NMDA: 0.17±0.36 p = 3.6534×10^{-4} Normal textures (post-injection) Sham: 3.29±0.50 NMDA: 1.87±0.58 p = 5.0056×10^{-4} p NMDA inverted vs. normal = 2.4831e-04 p Sham inverted vs. normal = 0.0886 *p-values are Bonferroni corrected*	two-tailed Wilcoxon rank sum test
S4b	Backlights on vs. backlights off	F-statistic = 0.009, p = 0.926, 95%CI of the true mean difference = [-0.728; 0.488]	repeated measures anova
S4c	Two vs. one wing remaining	t-statistic = 8.9381, p = 3.1088×10^{-8}, 95%CI of the true mean difference = [1.3640; 2.1982]	two-tailed, paired t-test
S4e	Proportion of trials with performance drop	Mean ± 95%CI Control: 0.28 ± 0.01 Ablated: 0.21 ± 0.03 p = 0.0286	two-tailed Wilcoxon rank sum test
S4f	Residuals of the sigmoidal fit in ablated and native mice	Median [IQR] Control: 0.15 [0.07;0.27] Ablated: 0.26 [0.10; 0.44] Mean ± 95%CI Control: 0.1909 ± 0.0058 Ablated: 0.2849 ± 0.0036 p = 3.2132×10^{-96}	two-tailed Wilcoxon rank sum test
S4g	Averaged whisker angles during wide and narrow trials	Significant time window, with Bonferroni correction, starting at 70 ms after trigger onset.	Welch's t-test
S5	Firing rates during quiescence and whisking	Significantly enhanced cells: 60 (BC), 101 (VPM), 81 (POm), 36 (ZIv) Significantly suppressed cells: 20 (BC), 6 (VPM), 2 (POm), 5 (ZIv) Mean quiescence firing rate [Hz]: 13.43 (BC), 16.13 (VPM), 18.53 (POm), 13.74 (ZIv) Mean whisking firing rate [Hz]: 16.96 (BC), 23.76 (VPM), 27.45 (POm), 19.08 (ZIv) p = 2.7496×10^{-16} (BC), 1.1239×10^{-46} (VPM), 2.1961×10^{-35} (POm), 7.5269×10^{-16} (ZIv)	two-tailed paired t-test

Supplementary table 1. Description of statistical parameters.